NANO · MICRO small
www.small-journal.com

Oxygen Vacancy-Tailored Schottky Heterojunction Activates Interface Dipole Amplification and Carrier Inversion for High-Performance Potassium-Ion Batteries

*Yi-Yen Hsieh and Hsing-Yu Tuan**

An oxygen vacancy-tailored Schottky heterostructure composed of polyvinylpyrrolidone-assisted $Bi_2Sn_2O_7$ (PVPBSO) nanocrystals and moderate work function graphene (mWFG, WF = 4.36 eV) is designed, which in turn intensifies the built-in voltage and interface dipole across the space charge region (SCR), leading to the inversion of majority carriers for facilitating K^+ transport/diffusion behaviors. Thorough band-alignment experiments and interface simulations reveal the dynamics between deficient BSO and mWFG, and how charge redistribution within the SCR leads to carrier inversion, demonstrating the impact of different defect engineering degrees on the amplification of Schottky junctions. The ordered transport of bipolar carriers can boost electrons and K ions easily passing through the inner and outer surfaces of the heterostructure. With high activity and low resistance in electrochemical reactions, the PVPBSO/mWFG exhibits an attractive capacity of 430 mA h g^{-1} and a rate capability exceeding 2000 mA g^{-1}, accompanied by minimal polarization and efficient utilization of conversion-alloying reactions. The substantial cell capacity and high-redox plateau of PVPBSO/mWFG//PB contribute to the practical feasibility of high-energy full batteries, offering long-cycle retention and high-voltage output. This study emphasizes the direct importance of interface and junction engineering in improving the efficiency of diverse electrochemical kinetic and diffusion processes for potassium-ion batteries.

1. Introduction

Potassium-ion batteries (PIBs) have emerged as an ideal alternative to lithium-ion batteries (LIBs) and sodium-ion batteries (SIBs) due to its low manufacturing, material costs, the relatively low reduction potential of potassium (≈2.936 V vs the standard hydrogen electrode), electrochemical similarity with the established LIBs and SIBs, and potential applications for grid-scale energy storages. Although the standard redox potential of K^+/K is in between Li^+/Li (−3.040 V) and Na^+/Na (−2.714 V) couples, the redox potential of theoretical calculation in organic solvents, however, demonstrated that the K^+/K (−2.88 V) redox couple could exhibit lowest reduction potential like propylene carbonate as compared to Li^+/Li (≈2.79 V) and Na^+/Na (≈2.56 V).[1] This can lead to an attractive working window, resulting in sufficient energy density for KIBs in commercial application. Surprisingly, weak Lewis's acidity of K ions leads to the smallest Stokes' radius (K^+: 3.6 Å, Na^+: 4.6 Å, and Li^+: 4.8 Å) in organic solvents, which benefits ionic diffusivity. In addition, K ions can insert into the layer of graphite to form a KC_8 compound, with a theoretical capacity of ≈279 mA h g^{-1}, which is compatible with the Li-battery industry.[2] Therefore, PIBs are considered one of the most promising candidates for next-generation energy storage. However, the low redox plateaus and specific capacities of carbon materials would result in poor energy density.

Recently, the design of conversion-type electrodes, specifically those that incorporate oxides, sulfides, selenides, and phosphides have been found to potentially deliver a higher capacity and more consistent voltage plateaus compared to traditional carbon and alloy-based materials. However, the drawbacks of employing conversion-type anodes in PIBs still pose various difficulties, including severe volume variation, sluggish kinetic diffusion, and most importantly, the irreversibility of conversion species during the cycling process. Recent studies have proposed versatile design strategies to minimize side reactions and enhance the performances of PIBs, such as networks,[3] nanowires,[4,5] nanoparticles,[6–8] sheets,[9] and teardrops.[10] Moreover, depending on the combination of components and composites, promising synergistic effects between metals, metal-chalcogenides, and semiconductors-conductors have been achieved, owing to bond softening,[11] self-healing features,[12] entropy configuration,[13] stress relaxation,[14,15] shuttle inhabitation,[16] and mechanism synergies (e.g., intercalation-alloying,[17,18] conversion-alloying,[19] multiple conversion-transition metal[20,21]). Although nanotechnology and composite engineering have advanced alkali-ion batteries by improving their rate capability, cyclability, and structural integrity, optimizing electrochemical kinetics remains a

Y.-Y. Hsieh, H.-Y. Tuan
Department of Chemical Engineering
National Tsing Hua University
Hsinchu 30013, Taiwan
E-mail: hytuan@che.nthu.edu.tw

The ORCID identification number(s) for the author(s) of this article can be found under https://doi.org/10.1002/smll.202305342

DOI: 10.1002/smll.202305342

challenge. Factors like extreme polarization, irreversible changes in active materials, and substantial lattice distortion in heterostructures during charge and discharge cycles contribute to these difficulties. Conventional heterointerface engineering appears inadequate in addressing the limitations of conversion-type materials for potassium-ion storage.[22,23] To overcome these issues, it is crucial to fine-tune the relationship between the band structures of semiconductors and conductors. This process will help create a built-in electric field and form a bipolar junction, which will overcome the limitations and impedance in electrochemical kinetics. As a result, surface activity will be enhanced, and charge transport in solid-state materials will be accelerated by reducing diffusion barriers. However, without tuning the ordered transfer orientation and redistribution of electrons, the highly active materials would stuff uneven and severe redox reactions, accompanied by structural cracking and irreversibility. A robust active layer and simultaneously controlling the transfer direction of electrons is necessary to prevent material destruction and poor kinetic behaviors. Therefore, using Schottky contact may simultaneously possess these requirements.

Establishing an efficient Schottky junction is one way to regulate carriers mobility and enhance charge transfer in energy storages.[24,25] For instance, Schottky junction between n-type semiconductors and conductors transfers its carriers from the conduction band minimum (CBM) to the Fermi level of the conductor in the SCR. Utilizing Schottky heterojunctions between conductors and semiconductors to separate created carriers may effectively prevent carrier recombination and enhances surface reactivity with K^+. For example, Yajima et al. controlled the artificial interface dipole to insert a cation or anion into $SrRuO_3$/Nb:$SrTiO_3$ heterointerface, tuning the Schottky barrier height beyond a broad range, thus provides a compelling toolbox for oxide materials in a wide range of applications.[26] Harada et al. proposed a systematic variation of Schottky barriers in metal/$PdCoO_2$/β-Ga_2O_3 junctions with an insertion layer consisted of ionic Pd^+ and $[CoO_2]^-$, spontaneously inducing the interface dipoles and increasing barrier height.[27] Through modifying dangling bonds and O-containing functional groups, Lee et al. have designed a deep Schottky-barrier CCF-M coated on Zn foil, effectively increasing the corrosion resistance, dendrite suppression, and Zn ions transport ability.[28] These studies present effective strategies for amplifying the interface dipole between semiconductor and conductor, as well as tuning the Schottky barrier height and built-in voltage so as to amplify the Schottky effect. Therefore, the scenario to prevent side reactions during the cycling process of PIBs is to form a heterojunction between two materials and enhance the reversibility of K ions in the metal oxide. For this purpose, n-type ternary metal oxides were chosen as electron donors to form Schottky contacts with mWFG conductors because n-type semiconductors have higher electric conductivity, which can effectively catalyze the sp^2 vibration of graphene materials,[29] enhancing the electrochemical activity of whole materials with a reduced passivating property of oxides. Notably, due to highly dispersed electronic structures and hybridized interactions of ternary ABO compound,[30] CBM and valence band maximum (VBM) edges of $Bi_2Sn_2O_7$ can improve the mobility of holes and electrons, easily enhancing the reactivity with surfactants and producing the deficient surface. Therefore, choosing these ABO compounds can effectively tune their work function (WF), Fermi level, bandgap, and carrier concentration via defect engineering. Also, controlling the layered structure of graphite is one way to tune the WF of the conductor, tailoring the n-type deficient semiconductors.

Typically, effectively controlling the interface dipole can establish sufficient built-in voltage and Schottky barrier. To accurately control the interface dipole using oxygen vacancies (OVs), the most adaptable strategy involves reducing particle size and increasing exposed facets to create digging bonds and unpaired electrons. Beyond high-temperature operation, utilizing surfactants to modify interface chemistry has emerged as the main approach for conducting defect engineering. The surfactant ligands are capable of forming complexes with metal cations, leading to unsaturated coordination of surface atoms and the presence of unpaired electrons. This results in a more negatively charged surface with enhanced reactivity, which readily interacts with cations or other materials. Schottky barrier (Φ_{SB}) significantly influences the performance of Schottky heterostructures, enabling a direct estimation of barrier height by examining the intrinsic properties of the two contacting materials in n-type semiconductors through photoemission techniques. The Schottky junction forms in n-type semiconducting materials when the WF of conductor is positioned within the semiconductor bandgap region and is smaller than the WF of semiconductor. According to modification Mott-Schottky mode for n-type semiconductor.[31,32]

$$\Phi_{SB} = \Psi_c - \chi_s + \Delta V \quad (1)$$

where Ψ_c, χ_s, and ΔV are, respectively, WF of conductor, electron affinity (EA), and absolute value of interface dipole. Based on this, energy level alignment can be optimized by adjusting surface polarity and electronic properties, enabling carriers to be more easily excited and transferred to the active surface to participate in redox reactions during the cycling process. The ability to intentionally adjust interface dipoles remains a relatively uncharted avenue for metal oxides, leading to a stronger Schottky junction in PIBs.

In this study, we design a tailored Schottky heterostructure with polyvinylpyrrolidone (PVP)-induced OVs. The Schottky junction is amplified by the robust built-in voltage and interface dipole between defective PVPBSO and mWFG (**Scheme 1**a). This effective built-in electric field and carrier redistribution reinforce the heterojunction effect, resulting in excellent electrochemical kinetics and diffusion capabilities for electrons and potassium ions. A comprehensive analysis of energy-level alignments and calculations for both perfect and defective BSO reveals significant differences in semiconducting properties. The absence of high-electronegativity oxygen atoms increases unpaired electron density and reduces the electrophilic property of the BSO surface (Scheme 1b,c). Due to effective defect modulation, the amplified interface dipole, combined with a strong built-in voltage, enhances the donor capability to conductors, significantly improving the Schottky junction and barrier. An inversion regime of majority carriers across the SCR occurs in oxygen vacancy-induced BSO/mWFG (Ov-BSO/mWFG), without electron tunneling phenomena (Scheme 1d,e). In contrast, inadequate band bending/interface dipole in perfect lattice-BSO/mWFG (Perfect-BSO/mWFG) leads to electron tunneling and recombination, reducing electrochemical reactivity and charge transport flux.

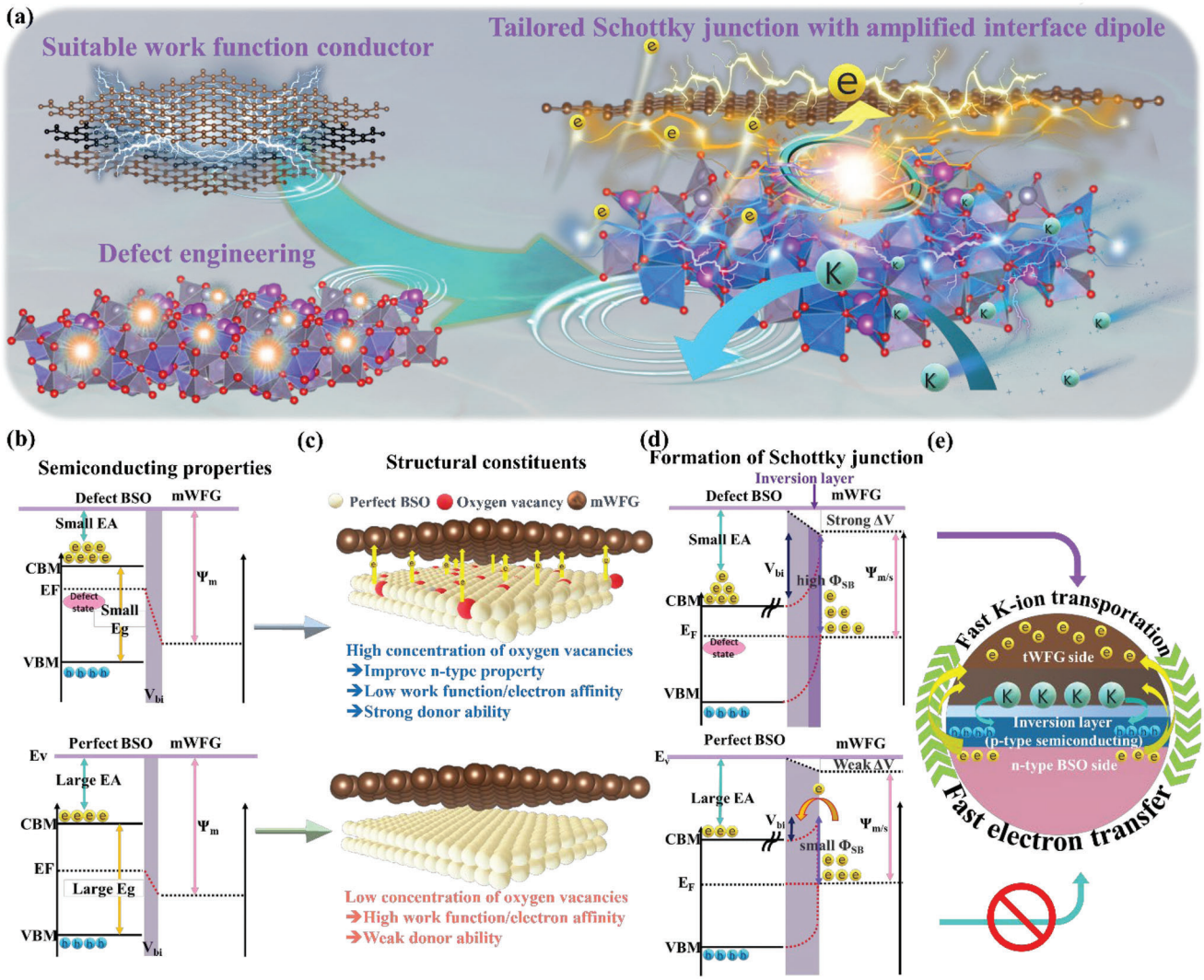

Scheme 1. Schematic illustration of band alignments and working mechanism of Schottky junction with defect engineering. a) Synergistic enhancements of electrochemical kinetics with tailored Schottky junction for interface dipole amplification. b) Energy-level diagrams of defect BSO/mWFG and Perfect-BSO/mWFG before contacting. c) Schematic illustration of the electron transfer direction and interfacial properties of defect BSO and Perfect-BSO contacted with mWFG. d) Scheme of Schottky junction formation with different interface dipole, band bending, built-in voltage, tunneling effect, and Schottky barriers between defect BSO/mWFG and Perfect-BSO/mWFG. e) Influence of inversion phenomenon after Schottky heterojunction formation in PVPBSO/mWFG and BulkBSO/mWFG. Notes: (Ψ), Schottky barrier (Φ_{SB}), built-in voltage (V_{bi}), interface dipole (ΔV) of (h) PVPBSO/mWFG and (i) BulkBSO/mWFG after contacting. Φ_{SB}, Schottky barrier; V_{bi}, built-in voltage; E_v, vacuum level; CBM, conduction band minimum; and VBM, valence band maximum.

Consequently, the Schottky heterostructure offers enhanced electrical and ionic conductivity, as well as increased kinetic dynamism, accelerating electrochemical performance in PIBs.

2. Results and Discussion

2.1. Material Characterization and Simulation for Deficient Architecture and Oxygen Vacancies

The PVP polymers can give both hydrophilic and hydrophobic functional groups for manipulating the defect structure and interface, such as donor ability of C═C and electrostatic force of long C—C chain. The hydrophilic group can serve as an electron donor, stabilizing the high surface energy of BSO precursor and partially reducing the surface atoms. The long chain of alkanes in PVP molecules can effectively form a micelle, and it can prevent the BSO nucleus from aggregating and further normalize the particle size. Besides, we synthesized the non-PVP-added BSO (nP-BSO) to compare with PVPBSO and BulkBSO in this work. The detailed scheme, characterization, and analysis are shown in Supporting Information (see Note S1 and Figure S1, Supporting Information). **Figure 1**a shows the high-resolution transmission electron microscopy (HRTEM) image displaying a uniform and sub-10 nm PVPBSO synthesized from a hydrothermal synthesis, while corresponding fast Fourier transformation (FFT) patterns indicate the exposed facets of (010) diffracted from six crystal

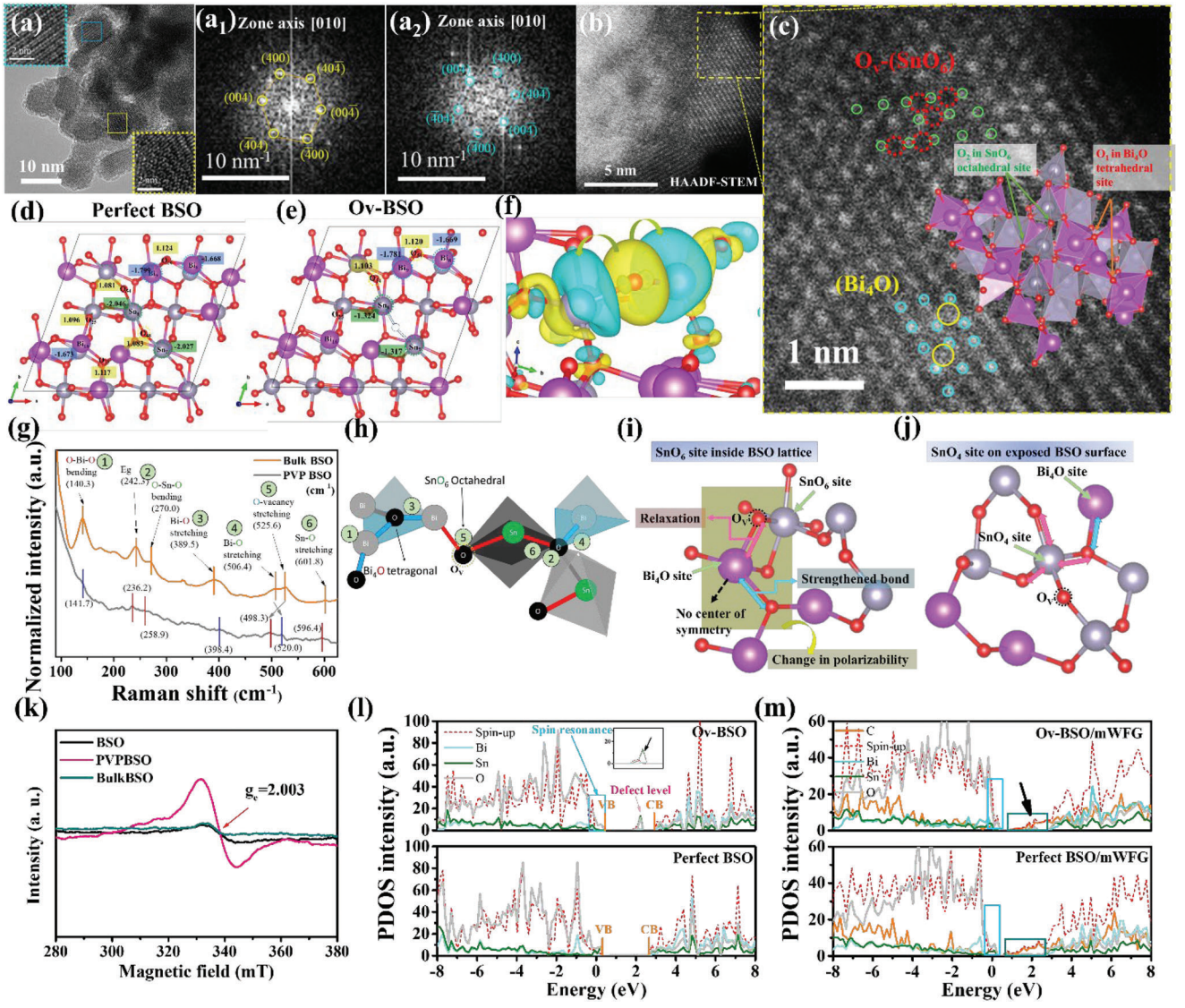

Figure 1. Characterization and DFT calculation of oxygen vacancies and corresponding impacts on BSO crystal lattice. a) HRTEM images of PVPBSO with enlarged insets of lattice fringes and corresponding FFT patterns of (010) planes. b) HAADF-STEM image and c) magnified image of PVPBSO with monoclinic crystal structure consisting of (Bi_4O) and (SnO_6) polyhedral. Bader charge analysis of d) Perfect-BSO and e) Ov-BSO (removal of one oxygen atom) with losing or gaining electrons of Bi (blue), Sn (green), and O (yellow). f) Charge density difference of O and Sn atoms in defect site of BSO surround by blue region (depletion) and yellow region (accumulation). g) Raman spectrum of BulkBSO and PVPBSO with h) corresponding position of vibration modes. i,j) The variation of interaction force at SnO_6 polyhedral site as OV formed inside BSO lattice and on exposed surface, respectively. k) EPR spectrum of PVPBSO, BulkBSO, and BSO. l,m) PDOS simulation of Ov-BSO and Perfect-BSO, Ov-BSO/mWFG and Perfect-BSO/mWFG, respectively.

orientation of [400], [004], [−404], [−400], [00−4], and [40−4], and it can be fitted in accordance with the monoclinic unit cell based on Bragg's law (Figure 1a). The *d*-spacing of lattice planes are 2.69, 3.08, and 3.09 Å relative to (400), (004), and (40−4) facet, as given in Figure S7 (Supporting Information). The X-ray photoelectron spectroscopy (XPS) was used to determine the effect of OVs and Schottky heterostructures for characterizing the binding energy (BE) changes with electron density around surface of materials (Note S2, Supporting Information). By effectively controlling and stabilizing the exposed surface with PVP surfactant, the Sn-adjacent OV structure occurs in PVPBSO, increasing the electron density of Sn atoms in the valence band (VB). Along with the abundance of valence electrons, the ionization energy of PVPBSO is reduced, consequently lowering the binding energy of Sn. The high-angle annular dark field scanning transmission electron microscope (HAADF-STEM) images in Figure 1b,c demonstrate the different degree of brightness between SnO_6 and Bi_4O unit consisted of octahedral and tetragonal sites, respectively, in tandem with the brightness difference surrounding the metal atoms. The red dashed circles in SnO_6 shows the OVs adjacent to Sn atoms, while yellow circles in Bi_4O represent the existence of oxygen atoms. Furthermore, the OVs and color changes of PVPBSO demonstrated that the crystallographic defects emerged on the surface after the surface mediation, in line

with the previous literature using heat-treatment process in a He atmosphere.[33]

To get a deep insight into OVs position on the exposed surface of BSO, the models of density functional theory (DFT) are constructed to investigate the dissociation feasibility. (Note S3, Supporting Information) Positive and negative charges in Bader analysis of Perfect-BSO represent the gain and loss of electrons, while the yellow, green, and blue regions are assigned as charge variation of O, Sn, and Bi atom, respectively (Figure 1d). As an oxygen atom gains more electrons, the interaction between metal and oxygen becomes stronger. Focusing on O_{48} (Sn—O—Sn), O_{56} (Bi—O—Bi), and O_{25} (Sn—O—Bi), the fewer charges gained by O_{48} indicate a weaker interaction between Sn and O at the exposed surface of SnO_4 site. This confirms that the formation of an OV structure through the dissociation of the Sn—O bond is easier than that through the Bi—O bond. When the OV is formed (Figure 1e), two Sn atoms connected to O_{48} would gain electrons owing to charge redistribution of BSO surface with loss of high electronegativity (EN) of O atom. The charge density difference (CDD) simulation can visually present the electron accumulation (yellow region) and depletion (blue region). The intense electrons are accumulated in the removed O, implying that the larger electron transport would be induced as the O is removed from the BSO molecular structure (Figure 1f). When the O is removed from the BSO, the electrons are transferred to the Sn atoms on both sides of the O atom. The Sn atoms, therefore, would obtain the higher electron density, which is consistent with XPS results. Furthermore, the signals of Raman spectrum and X-ray diffraction (XRD) pattern of PVPBSO turn into broader and peak intensity decreased as the crystal size decreased.[34] Once the surface vacancies are formed, an asymmetric vibration behavior related to deficient region elaborated that some atoms on the surface lacked adjacent atoms with formation of dinging bonds. According to the Bager's rule, there is a negative correlation between stretching frequencies and bond length. Because of structural softening and strengthening, the Raman active band would be shifted with change of polarizability. Therefore, the relaxation and compression of metal–oxygen bond could further clarify the existence of OV structures. Compared to the Raman shift of BulkBSO and previous literatures,[35,36] normalized intensity of Raman spectrum and vibration position are shown in Figure 1g,h, Figure S9 and Table S1 (Supporting Information). The blueshift of Bi—O bending (1) and stretching (3) suggests strengthened bonds in the Bi_4O framework, while the redshift of both Sn—O vibration modes and its nearest OV stretching due to lattice relaxation. Meanwhile, the Bi-O stretching (4) aligned with the O atoms in SnO_6 polyhedral is blueshift no matter what the Bi atoms connect with SnO_4 or SnO_6 sites. Nevertheless, when the nonlayered structure of BSO exposed the specific lattice facet, the coordination of metal atoms would be different from those inside the unit cell. Therefore, we construct two modes of deficient lattice on basis of Sn-adjacent vacancies to evaluate the possible variation of bond length. Two different coordinated environments indicate that there are six and four O atoms coupled with one Sn atom, respectively (Figure 1i,j and Figure S10, Supporting Information). The binding strength on Bi-adjacent covalent bonds (Bi_9—O_{31} and Bi_{16}—O_{29}) is enhanced, whereas the Sn—O vibration modes are relaxed due to weak binding ability and Sn-adjacent vacancy, in accordance with Raman vibration variation. Besides, the redshift of E_g vibration mode also demonstrates that the PVPBSO architecture would be softened due to abundant defect sites. Both experiments and simulations testify that site-selective OVs would be formed at Bi—O—SnO_5 and Sn—O_4 site rather than Bi_4O site.

Electron paramagnetic resonance (EPR) spectrum can directly collect the electron spin resonance emitted by unpaired electrons on basis of the Zeeman effect (Note S4, Supporting Information). The unpaired electron resonance of PVPBSO at g-value of 2.003 is much stronger than BSO and BulkBSO, confirming that more OVs are exposed on the surface of PVPBSO (Figure 1k). The inclusion of PVP is a crucial step in adjusting the OVs on the PVPBSO surface, which is further emphasized by the low coordination of metal ions. The partial density of states (PDOS) can provide evidence for validating the impact of vacancies and the Schottky heterojunction. Two valence electrons are formed with removal of one O atom from Sn-adjacent sites, giving a strong spin-up resonance at VB edge in Figure 1l-top. According to the Hund's rule, the p-orbital of each Sn atom near deficient site could be filled with one spin-up electron, leading to half-full orbital with three spin-up electrons in each same level of orbital before pairing up. The DOS intensity at VB edge indicates that there is absence of Sn-O bond on Ov-BSO surface compared to those on Perfect-BSO. Furthermore, the presence of OVs structure increases the DOS intensity of conduction band (CB) edge, thus improving the driving force of electron transport through the deficient surface.[37] Furthermore, a defect level exists within the bandgap of Ov-BSO, close to the CB edge, contributed by Sn and O (inset of Figure 1l-top). This defect level reduces the energy gap and the recombination rate of electrons and holes, consequently enhancing electron migration to the Fermi level of the conductor. In contrast to Perfect-BSO, the downshift of CB edge of Ov-BSO/mWFG elaborates a strong coupling between Ov-BSO and mWFG due to the donor ability of defect sites (black arrow) and abundant valence electrons (Figure 1m).

2.2. Heterostructure Characterization for Schottky Junction and Energy Level Alignments

The WF of mWFG is 4.36 eV compared to that of traditional graphite (>4.7 eV) and few-layered graphene (<4.2 eV) (see Note S5, Supporting Information).[38,39] The nanosized grains of PVPBSO are well-dispersed in mWFG layers given in **Figure 2**a,b. The main exposed and contact facet of PVPBSO and mWFG are respectively (010) and (002) crystal faces. The Schottky interface of PVPBSO/mWFG heterostructure can be exhibited a well-contacted heterograin boundary between PVPBSO and mWFG. The HRTEM image and FFT analysis (Figure 2c,d and Figure S16, Supporting Information) demonstrate a clear atom arrangement in (010) facet of PVPBSO/mWFG monoclinic lattice with beta angle of 125°, consistent with HRTEM results of bare PVPBSO. In addition, the [001] orientation and lattice fringes of mWFG are a preferential and stable phase to closely contact with (010) facet of PVPBSO, therefore being used in the simulation models of Schottky heterostructure. The detailed XPS, Raman, and TGA analysis of PVPBSO/mWFG and BulkBSO/mWFG are shown in Note S6 (Supporting Information). Due to present of sp^2 vibration, the loss and gain of

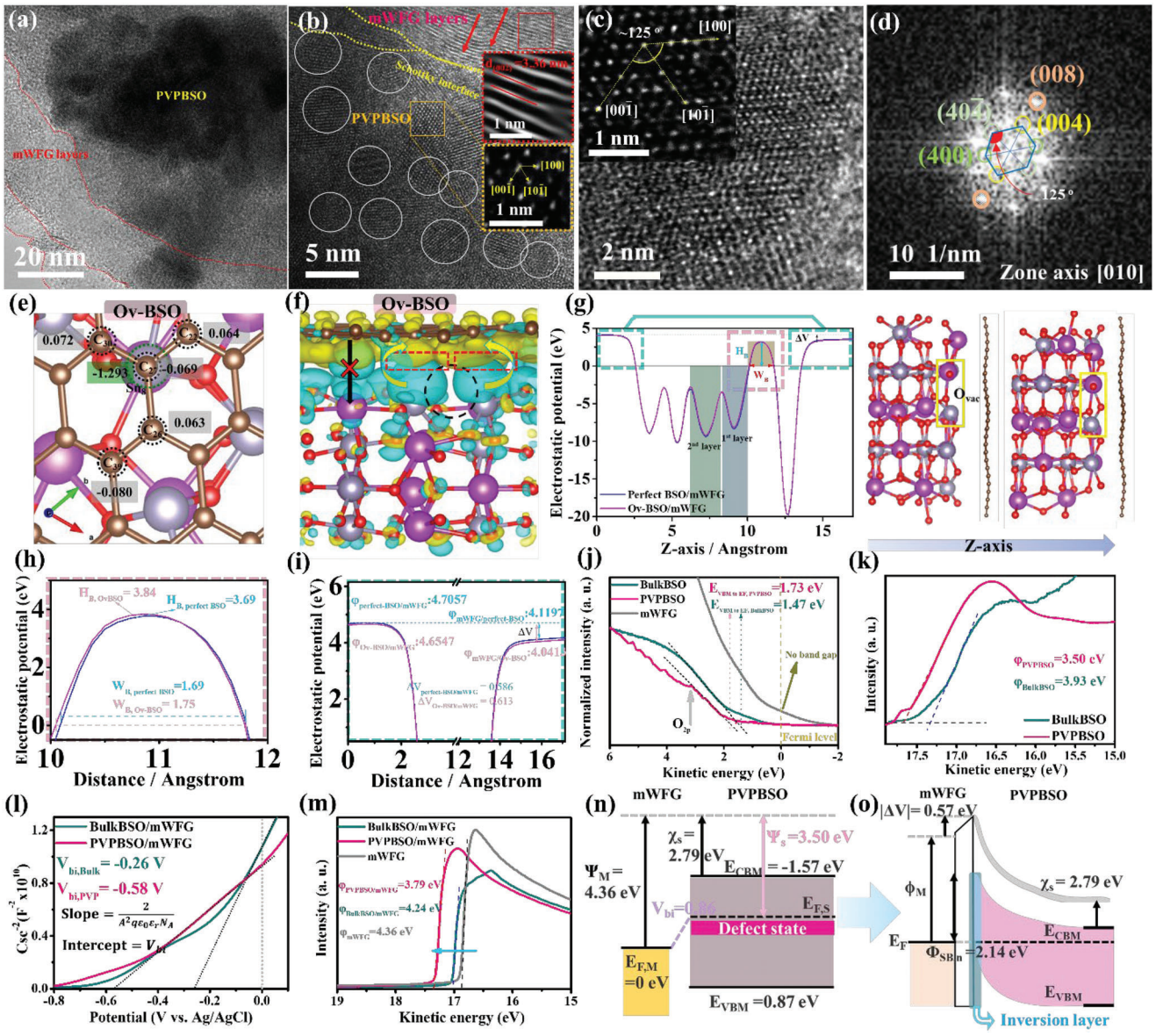

Figure 2. Simulations and photoemission experiments for band alignments and Schottky junction. a–c) HRTEM images and d) corresponding FFT and iFFT analysis of PVPBSO/mWFG. e) Bader charge analysis and f) Charge density difference of Ov-BSO/mWFG. g) Electrostatic potential and related stacking directions of Perfect-BSO/mWFG and Ov-BSO/mWFG along with enlarged h) interface barrier and i) interface dipole. j) Low kinetic energy and k) high kinetic energy regions of UPS spectrum before contacting. l) Mott–Schottky plot of PVPBSO/mWFG and BulkBSO/mWFG. m) high KE region of UPS spectrum after forming heterostructures. The calculated band alignments of PVPBSO/mWFG n) before and o) after contacting.

electrons in mWFG layer would be simultaneously have been demonstrated in Figure 2e. Consistent with Bader analysis of Ov-BSO without heteromodel construction, the Sn atom of Ov-BSO gains many electrons after removing an O atom. Notably, the overall C atoms of mWFG near OVs site also obtain electrons transferred from Ov-BSO, including the C atom on the top of OVs site and Sn atom. To graphically observe the charge transfer between mWFG and BSO, the CDD of BSO/mWFG are shown in Figure 2f. Because of the lower EN of Sn than that of O, the electron-gaining Sn atoms of Ov-BSO could serve as a donor and much easier to contribute the electrons to mWFG than other atoms in BSO. It is worth noting that Sn atoms of Ov-BSO have a large contact area with the electron cloud of mWFG on the condition of removing O atoms (red dash line). As Ov-BSO is formed, more effective electron transfer from BSO to mWFG is induced without a tunneling phenomenon owing to stronger Schottky effect. The detail descriptions of Perfect-BSO /mWFG simulation are given in supporting information (Figure S17, Supporting Information).

To further confirm the charge transfer behavior, an electrostatic potential (ESP) analyses are performed to investigate the interfacial interaction and built-in electric field of the PVPBSO/mWFG heterostructure (Figure 2g). Given the consistency of nucleus positive charge, the higher potential energy

indicates the absence of negative charges, which would mean that there are fewer electrons in this region. The converse is also true.[40] Thus, a high ESP indicates the relative absence of electrons and a low ESP indicates an abundance of electrons.[41] The reduced electrophilicity of Ov-BSO augments electron transfer, enabling charge redistribution across the top two layers of the BSO surface when vacancies occur.[42] It is obvious that a large ESP difference between the BSO and mWFG in the heterostructure, implying that there is a strong electrostatic field and electron transfer between the mWFG and BSO. As the Schottky heterointerface are constructed, the electrons on BSO surface would be attracted by the high-ESP mWFG, forming n-type Schottky heterostructure. When the electrons of semiconductors effectively transfer to the flat band of conductor until Fermi level of both materials are equilibrium, the BSO-terminated WF of heterostructure would increase with decreased electron density in accordance with the XPS data. Importantly, interface dipoles are related to the built-in voltage, while the Schottky barriers are corresponded to the W_B and H_B. The W_B and H_B of Ov-BSO/mWFG (3.84 eV/1.75 Å) are larger than those of Perfect-BSO (Figure 2h). Therefore, the T_B of Ov-BSO is smaller than that of Perfect-BSO based on tunneling probability equation (Note S7, Supporting Information), confirming that the OV structures could improve the Schottky barrier and hinder the electron tunneling. Furthermore, the simulated interface dipole (ΔV) is essentially determined by the strength of the charge transfer.[43] The ΔV, driving force of charge transfer, is alternately obtained through the potential difference between the ESP of both states in the vacuum level (Figure 2i). The potential difference of the vacuum level between two polar surfaces (ΔV) in the ESP simulation, namely, interface dipole, becomes more notable with the defect forming.[44] As a result, the interlayer coupling and Schottky junction between Ov-BSO and mWFG are strengthened, leading to an increased transfer of electrons from BSO to mWFG and enlargement of ΔV. As contacted with mWFG, the large difference of ΔV between two materials leads to strong driving force of free electrons transferred from BSO to mWFG with the gradual presence of interface polarization between n-type BSO and mWFG. After finishing the majority carrier transfer, the CDD simulation in Figure 2f displayed that the electrons would be accumulated in mWFG layer, and the electron depletion happened at the BSO surface. Due to the accumulation of negative charges near the heterointerface of mWFG, there is a nonuniform electric field, leading to interface polarization between Ov-BSO and mWFG. After equilibration, the accumulated electrons raise the interfacial electron concentration, enhancing the electrochemical performance of PVPBSO/mWFG.

UPS spectra offer key evidence to ascertain the relative locations of various energy levels, helping to perform a thorough experimental evaluation of band alignment. In low kinetic energy (KE) region (Figure 2j), the VBM edges for PVPBSO and BulkBSO are 1.73 and 1.47 eV relative to their E_F, respectively. Specifically, the presence of an OV on the BSO surface would result in a distinct O 2p band, centered at ≈3.0–3.5 eV.[45] As the defect state is close to the CBM edge, the carrier density would increase, giving rise to an upshift of E_F. Notably, the mWFG has no bandgap due to Fermi level covered by VBM edge, therefore, it is a conductor. Focusing on cutoff point of high KE region (Figure 2k), the WF of PVPBSO, BulkBSO, and mWFG are 3.50, 3.93, and 4.36 eV, respectively. The PVPBSO/mWFG exhibits the minimum energy needed to remove an electron from a solid to the vacuum field. For the purpose of identifying n-type semiconductor, the bandgap of the PVPBSO and BulkBSO are estimated based on the Tauc's plot to be 2.44 and 2.56 eV (Figure S18a and Note S8, Supporting Information). Furthermore, the absorption edge of PVPBSO exhibits a redshift (indicated by the red arrow), emphasizing the crucial role of OVs in narrowing the bandgap (Figure S18b and Note S9, Supporting Information). On the basis of photospectroscopy measurements and Anderson's rule, the band diagrams are displayed in Figure 2p and Figure S17 (Supporting Information). The EA of semiconductors could be assigned by ESP simulation and the distance between E_{vac} and CBM edge derived by the experimental results (Figure S18, Supporting Information). The EA of Ov-BSO ($\chi_{simulation}/\chi_{experiment}$ = 2.43/2.79 eV) is smaller than that of Perfect-BSO, meaning that energy required for removing an electron from Ov-BSO is smaller than those of prefect BSO. In addition, a smaller slope in the Mott–Schottky (MS) plot corresponds to higher acceptor concentrations (N_A) and built-in potentials (V_{bi}) (Figure 2l and Note S10, Supporting Information). Hence, the significant band bending propensity and increased electron transfer between PVPBSO and mWFG are consistent with the analogous trend found in V_{bi} values derived from UPS and UV–vis experiments.

Thereafter, different Fermi level positions of two materials would lead to a spontaneous electron transfer as soon as they contact. Type inversion of semiconductor occurs if, with an n-type semiconductor, the density of holes in the SCR exceeds that of the electrons.[46] To prove this inversion regime, the band bending of inversion layer (BB_{inv}) of PVPBSO/mWFG are calculated to be 0.57, which is larger than $E_g/2 - \xi$ (Note S11, Supporting Information). Clearly, the hole density is much higher than that of electrons in the SCR, suggesting that the PVPBSO surface in contact with mWFG exhibits an inverted p-type semiconducting behavior. While a p-n junction caused by strong inversion is not expected in this case, these hole carriers can still facilitate K-ion transport within the interface, leading to higher ionic conductivity. As a consequence of the OV structures and inversion layer formation on the PVPBSO surface, the interface dipole, arising from electron density rearrangement at the Schottky interface, is established and calculated based on the electron vacuum level shift between mWFG and the PVPBSO/mWFG composite,[47] in accordance with tendency of ESP simulation. The WF of mWFG before and after placing in contact with PVPBSO/mWFG show the distinct trend of upshift from 4.36 to 3.79, which is larger than those of BulkBSO/mWFG (Figure 2m). The difference in Fermi level prompts the injection of electrons from BSO to mWFG, resulting in a reduced WF of mWFG. The upshifted Fermi level of n-type BSO, which is resulted from the OV-induced defect state, would strengthen the electron donor ability from CB of BSO to Fermi level of mWFG. As the electron density of CB of BSO is reduced, the Fermi level of BSO will downshift and eventually reach equilibrium with that of mWFG. Accordingly, the WF of BSO and mWFG would increase and decrease, respectively, which are consistent with UPS results. Moreover, the WF of the heterostructures is determined by the influence of BSO on the WF of mWFG, rather than the impact of mWFG on the WF of BSO. This is ascertained through the similar shape and

intensity of the high-KE region, as well as bandgaps relative to the UPS and Tauc's plot of pure mWFG (Figure S20, Supporting Information). Consequently, a strong spontaneous built-in electric field forms between PVPBSO and mWFG due to the lower EA and WF resulting from the abundant OV structure and electron density. As the heterointerface polarization induced by the behavior of electron transfer from BSO to mWFG, the density of majority carriers (e^-) of n-type BSO near SCR would be lower than that of minority carriers (h^+). According to the experimental results and calculation, the electrons transferred to mWFG would not be tunneled back to BSO due to the significant Schottky barrier between BSO and mWFG. Band alignment and associated calculations show that the substantial Schottky barrier prevents these electrons from tunneling back to PVPBSO according to the tunneling probability equation (Note S7, Supporting Information). Therefore, during the initial discharge process, K ions adsorb onto the electron-laden mWFG surface, resulting in interface polarization from electron carrier accumulation. When the density of majority carriers (electron) in the SCR of n-type PVPBSO declines below that of hole carriers, p-type semiconductor attributes emerge nearby. Thus, K ions from mWFG disperse further onto the n-type PVPBSO surface due to the high-density hole carriers from the type-inversion layer. Based on the modified MS equation, the Schottky barrier of PVPBSO/mWFG and BulkBSO/mWFG is 2.14 and 1.60 eV, respectively. As depicted in Figure 2o, an upward bending of energy bands in both BSO and an electric field pointing from BSO to mWFG persist, creating a Schottky heterostructure. The rectifying Schottky behavior significantly contributes to a powerful driving force for electron transfer from the CB of BSO to the Fermi level of mWFG without electron tunneling, prompting the oriented migration and transfer efficiency of electrons from BSO to mWFG. Subsequently, the enhanced interface dipole and built-in voltage induces an inversion layer, improving K-ion diffusion through the interface and achieving a spatially optimized distribution of charged species. In addition to interface polarization, the Schottky barrier is an important factor to reducing the probability of electron tunneling and maintaining the polar surfaces. The synergy of interface polarization and Schottky barrier can effectively promote an inversion layer of n-type BSO based on the related equation, facilitating the K ion transportation through the heterointerface and achieving a spatially optimized distribution of charged species. (Note S12, Supporting Information)

2.3. Electrochemical Performances and Impacts of Schottky Heterostructures on PIBs

The electrochemical behaviors of the PVPBSO/mWFG electrode were investigated in **Figure 3**. As cycled at a low current density of 50 mA g^{-1} after 200 times, the PVPBSO/mWFG delivers a reversible capacity of ≈430 mA h g^{-1}, being beneficial with better reactivity and reversibility induced by effective charge redistribution. Conversely, the progressively decay and sub-400 mA h g^{-1} capacities of BulkBSO, BulkBSO/mWFG, nP-BSO, and nP-BSO/mWFG are given in Figure 3a. Notably, the effective Schottky heterojunction enhances uniform charge distribution, further improving the adsorption, insertion, and diffusion capabilities of K ions surrounding the conductive surface and inside the active space of BSO. To testify the improvement of electrochemical kinetics, the galvanostatic discharge–charge curves and enlarged voltage profiles are shown in Figure 3b–d, respectively. Initial K-ion adsorption and surface insertion occur above 1.5 V (yellow frame). The overpotential of the initial surface reaction and the flat slope of the plateau indicate that the activation barrier for the starting reduction reaction on the PVPBSO/mWFG surface is smaller than those on BulkBSO/mWFG and nP-BSO/mWFG. This suggests a uniform growth of the solid–electrolyte interface (SEI) layer with low polarization. In comparison to other materials without nanoengineering and vacancy engineering, the overpotentials of PVPBSO are smaller than nP-BSO and larger than BulkBSO. Owing to the reduced reactive area and inner surface of BulkBSO, the SEI layer growth on BulkBSO contributes a capacity of only 2 mA h g^{-1}. Although PVPBSO exhibits a lower overpotential than nP-BSO, its abundant surface area results in a prolonged reaction plateau for SEI growth with decreased initial coulombic efficiency (ICE = 60.6%). It's worth noting that a robust and uniform SEI film can reduce polarization, display a high discharge plateau, maintain cycling stability, and further prevent deformation/reformation of the SEI layer.[48,49] As the discharge ranges from 1.0 to 0.5 V (purple frame), PVPBSO/mWFG demonstrates great utilization of conversion-reaction species, delivering higher capacity with reduced side reactions compared to Schottky-free PVPBSO. The higher the energy barrier, the more challenging it becomes for a redox reaction to take place. Clearly, the conversion and alloying reactions of BulkBSO and BulkBSO/mWFG occur under the largest activation barrier and severe polarization (blue frame). Furthermore, to analyze electrochemical oxidation, the original voltage profiles are displayed in green and pink frames. Apart from the increased overpotential of BulkBSO, similar oxidation overpotentials of other materials are assigned in the green frame. While charging to 3.0 V (pink frame), the polarized curves of BulkBSO and BulkBSO/mWFG limit capacity performance due to the absence of interface and heterojunction engineering, thus inducing initial capacities with insufficient Schottky barriers and even ohmic junctions.

Upon pairing nP-BSO and BulkBSO with mWFG, their performance during the first cycle is negatively impacted compared to the pristine materials, as they display a reduced capacity relative to the original materials. However, PVPBSO/mWFG contributes a wide plateau and low polarization conditions, benefiting from enhanced electrochemical kinetics and better charge transport. Effective and controllable charge transfer helps reduce polarization caused by changes in electrochemical resistance and overpotentials. To verify cyclability and capacity retention with the impact of deficient structure and sufficient Schottky heterojunction, long-term cycling performances are shown in Figure 3e. After 1000 cycles at a current density of 500 mA h g^{-1}, only PVPBSO/mWFG retains its specific capacity over 200 mA h g^{-1} with a retention ratio of 81.4%. Notably, without suitable surface design, the Schottky junction and acquired p-type semiconducting property cannot be effectively inspired with transfer-expedited behaviors of both types of carriers. In other words, having an oriented transport path can facilitate electron redistribution and K-ion diffusion within the host material, thereby improving ionic/electric conductivity. As a result, both PVPBSO and BulkBSO/mWFG, with Schottky-free and weak Schottky contacts respectively, cannot stabilize

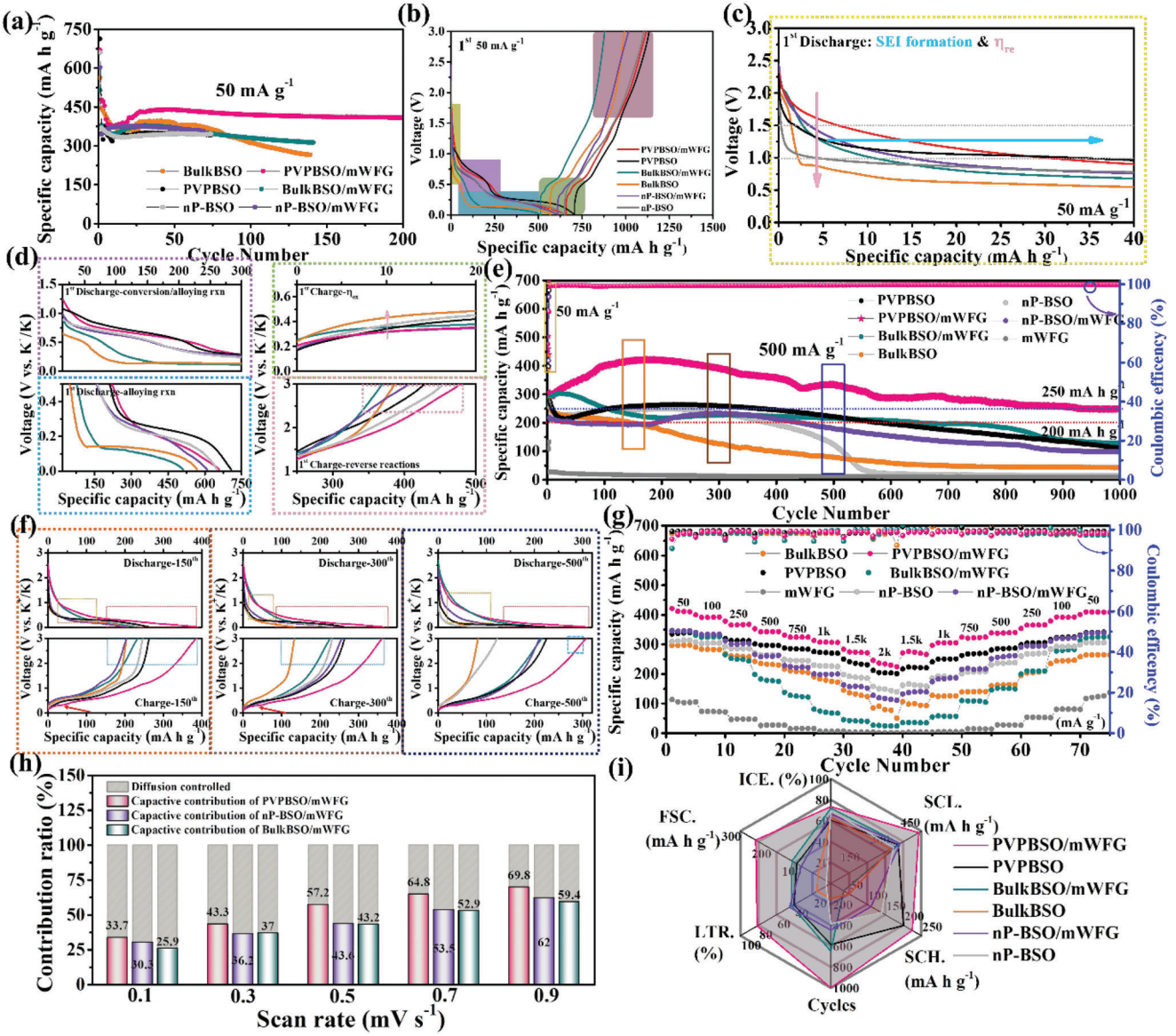

Figure 3. Electrochemical performances and analysis of PVPBSO/mWFG in PIB half cells. a) Cycling performance at a current density of 50 mA g^{-1}. b) Galvanostatic charge–discharge profiles for first at 50 mA g^{-1}. Enlarged area of the c) initial plateau (yellow region) and d) sequence regions of redox plateaus with their corresponding colors. e) Long-term cycling stability of PVPBSO/mWFG at 500 mA g^{-1}. f) GCD curves of PVPBSO/mWFG for 150th, 300th, 500th at current density of 500 mA g^{-1}. g) Rate performances of host materials and others in this work. h) Comparison of contribution ratio of surface kinetic-dominated and diffusion-dominated behaviors at various sweep rates. i) Comparison radar chart of initial Coulombic efficiency (ICE), cycle number, long-term retention (LTR), final specific capacity (FSC), low-current capacity at 50 mA g^{-1} (LCC), and high-current capacity at 500 mA g^{-1} (HCC) with other materials in this work.

ordered charge transfer and subsequent redox reactions. In addition, both BulkBSO (orange line) and nP-BSO (light gray line) demonstrate poor retention after 144 and 386 cycles, respectively. Despite being coupled with mWFG, these two materials only slightly improve cyclability, reaching 650 (dark cyan line) and 447 cycles (violet line), but with poor capacity contributions lower than 250 mA h g^{-1} (blue dashed line). As expected, the reversibility and reactivity of conversion-alloying products in PVPBSO/mWFG are superior to other materials in this work at subsequent cycles, illustrating the importance of constructing a well-tuned Schottky junction along with vacancy-mediated EA and interface dipole. There are activation states for PVPBSO/mWFG and nP-BSO/mWFG at the 150th and 300th cycles, respectively, suggesting effective Schottky heterojunctions coupled with an inversion layer. Due to the enhanced transfer ability of both electrons and ions, the materials gradually activate as the current density increases from 50 to 500 mA g^{-1}. As shown in the corresponding voltage profiles (Figure 3f), there is no conversion-reaction plateau present in BulkBSO, nP-BSO, PVPBSO, or nP-BSO/mWFG, while the conversion capacity of BulkBSO/mWFG remains half of that in PVPBSO/mWFG. The alloying plateau of PVPBSO/mWFG contributes to lower

overpotential and is almost double those of other materials. The dealloying/reverse conversion process of PVPBSO/mWFG also displays multiple reversed plateaus with lower polarization phenomena. The remaining overpotential and polarization of PVPBSO/mWFG maintain a higher reversible capacity than those of other materials at the 500th cycle. The rate capability is investigated from 0.1C to 4C (1C = 500 mA g^{-1}) to demonstrate the positive effect of Schottky heterojunction coupled with interface engineering on redox kinetics in Figure 3g. At stepwise cycling currents, the excellent rate performance of the host material is marked as 421, 393, 367, 343, 324, 306, 273, and 246 mA h g^{-1} at 50, 100, 250, 500, 750, 1000, 1500, and 2000 mA g^{-1}, respectively. Compared to PVPBSO/mWFG, the capacities of other anodes continuously decrease, and the capacity contributions of BulkBSO and BulkBSO/mWFG result in a sub-100 mA h g^{-1} capacity under high-current conditions. Similarly, BulkBSO/mWFG and nP-BSO/mWFG still perform worse than their pristine materials at high current densities due to the weak Schottky-junction effect. Without boosting carrier transport through strong synergy between hetero-interaction and vacancy engineering, the low capacities of other materials are observed at the first stage (50 mA g^{-1}). The exceptional storage performance and rate capability of K ions may be attributed to a combination of capacitive and diffusive behaviors. To initially confirm the merits of the Ov-amplified Schottky interface in PIBs, capacitive/diffusive contributions are testified with various sweeping rates of cyclic voltammetry (CV) from 0.1 to 0.9 mV s^{-1} (Figure 3h and Note S13, Supporting Information). The unchanged shape of curves, rather than the phase transition of bare materials in Figure S21 (Supporting Information), is observed.

A closed region of the CV curve at each scan rate (Figure S22, Supporting Information) shows the percentage of capacitive contribution relative to the total area is 69.8% at 0.9 mV s^{-1} for PVPBSO/mWFG, which is better than those of BulkBSO (59.4%) and nP-BSO (62.0%). When applied under fast charge/discharge conditions, the effective pseudo-capacitive behavior on the active surface could significantly support subsequent kinetic diffusion. As sweeping at 0.1 mV s^{-1}, the ratio of diffusion-controlled capacity of PVPBSO/mWFG is 66.3%, implying that many Faradaic reactions could be conducted and deliver higher capacity performance. Kinetic investigation using scan-rate-dependent CV tests provides a detailed analysis in accordance with rate performance. The PVPBSO/mWFG demonstrates attractive flexibility for mediating various current rates, leading to excellent rate capability at both low and high current densities. The comparison of the radar chart in six aspects, including ICE, cycle number, long-term retention (LTR), final specific capacity (FSC), low-current capacity at 50 mA g^{-1} (LCC), and high-current capacity at 500 mA g^{-1} (HCC), is displayed in Figure 3i, Figure S24 and Table S2 (Supporting Information). In addition, comparisons with other research articles mainly related to bismuth, antimony, tin-based oxide, and partially transition-metal oxides are presented. The ICE of most metal oxides in other literature is less than 60% with cycling retention lower than 75%. When cycling at high-rate current, the conversion reaction of metal oxides usually inherits an inevitable capacity loss and irreversible redox species. The PVPBSO/mWFG outperforms other anode materials in this study, exhibiting superior low-current capacity, high-current capacity, and long-term cyclability. Benefiting from Schottky junction and defect engineering, the reinforced electric and ionic networks are amplified to boost the orientated transportation of electrons and K ions.

2.4. Electrochemical Mechanism and Reversibility of $Bi_2Sn_2O_7$

The operando XRD contour plot is stacked alongside the voltage profile, illustrating the electrochemical evolution of PVPBSO/mWFG for the first three cycles at various voltage stages. The diffraction peaks at 28.8°, 33.2°, and 48.0° belong to PVPBSO before the cycling test, while the XRD signals of the stainless-steel operando holder consistently appear at 17.4°, 21.7°, and 24.1° (**Figure 4**a). As the K ions inserted into the anode material, the OCP suddenly dropped below 1.5 V, initiating the formation of solid–liquid phase and conversion reactions.

The characterization signals of the host anode progressively disappeared and accompanied with the formation of metal phases (Bi, Sn) and conversion species (K_2O_2, KO_2, K_2O). As continuously discharged to 0.5 V (blue region), the conversion-reaction signals of K_2O_2 and KO_2, and K_2O appear sequentially at 22.9° (JCPDS No. 00-032-0827) and 26.5° (JCPDS No. 00-039-0697), as well as 25.3° (JCPDS No. 01-077-2176). Simultaneously, the XRD contour signals located at 27.2° (JCPDS No. 00-044-1246) and 23.7° (JCPDS No. 00-005-0390) are assigned to the (012) plane of Bi and the (111) plane of Sn, respectively. Subsequently, the potassiation of Sn and Bi metal can gradually proceed through stage II (purple region) and stage III (green region), displaying the contour signals of KBi_2 (31.1/32.5°, JCPDS No. 04-010-8776), K_4Sn_{23} (27.7/30.6°, JCPDS No. 03-065-3351), K_3Bi (29.0/29.6°, JCPDS No. 04-007-3496), and KSn (28.6/29.7°, JCPDS No. 04-007-3503). Furthermore, post-mortem XPS and TEM techniques are adopted to confirm the operando XRD results. As initially discharged to 0.5 V (Figure 4b_1,c_1), there are two pairs of doublets of Bi^{3+} and Bi^0 with binding energy of 165.1/160 and 163.2/158.4 eV, being indexed as surface oxidation and KBi_2 alloy, respectively. The three pairs of doublet peaks of Sn^{4+} (498.0/488.7 eV), Sn^{4-2x} (495.6/487.1 eV), and Sn^0 (492.8/484.5 eV) 3d are associated with the SnO_2, SnO_{2-x}, and the alloy phase of K_4Sn_{23}, respectively. With the continuous insertion of K ions, the terminal alloying phases of K_3Bi and KSn have binding energies of 162/156.8 and 492.6/484.4 eV.

As the charging process begins, extracting K ions from potassiated species initiates the formation of dealloying phases, accompanied by the reversible alloying intermediates (KBi_2 and K_4Sn_{23}) and the subsequent metal phase. Following the generation of Bi and Sn metal, the potassium oxides begin the reverse conversion reactions to form the original BSO crystals. To distinguish the product at phase transformation between the first charging state and the second discharging state, we evaluate the ex situ XPS spectrum to provide cross-verification. As shown in **Figure 5**b_2,c_2, the binding energies of Bi (purple area) are 163.7/158.5 eV and 164.0/158.9 eV during charging to 2.25 and 3.0 V, implying that a lower oxidation state of Bi 4f exists in the product of charging to 2.25 V compared to those of charging back to 3.0 V. Moreover, compared with intensities of other ex-situ voltages, the intensity of Bi^{3+} at potentials of 3.0 V is much higher than that of the electrolyte, implying that the presence of BSO contributes to the intensity of Bi^{3+}. Specifically, Sn 3d

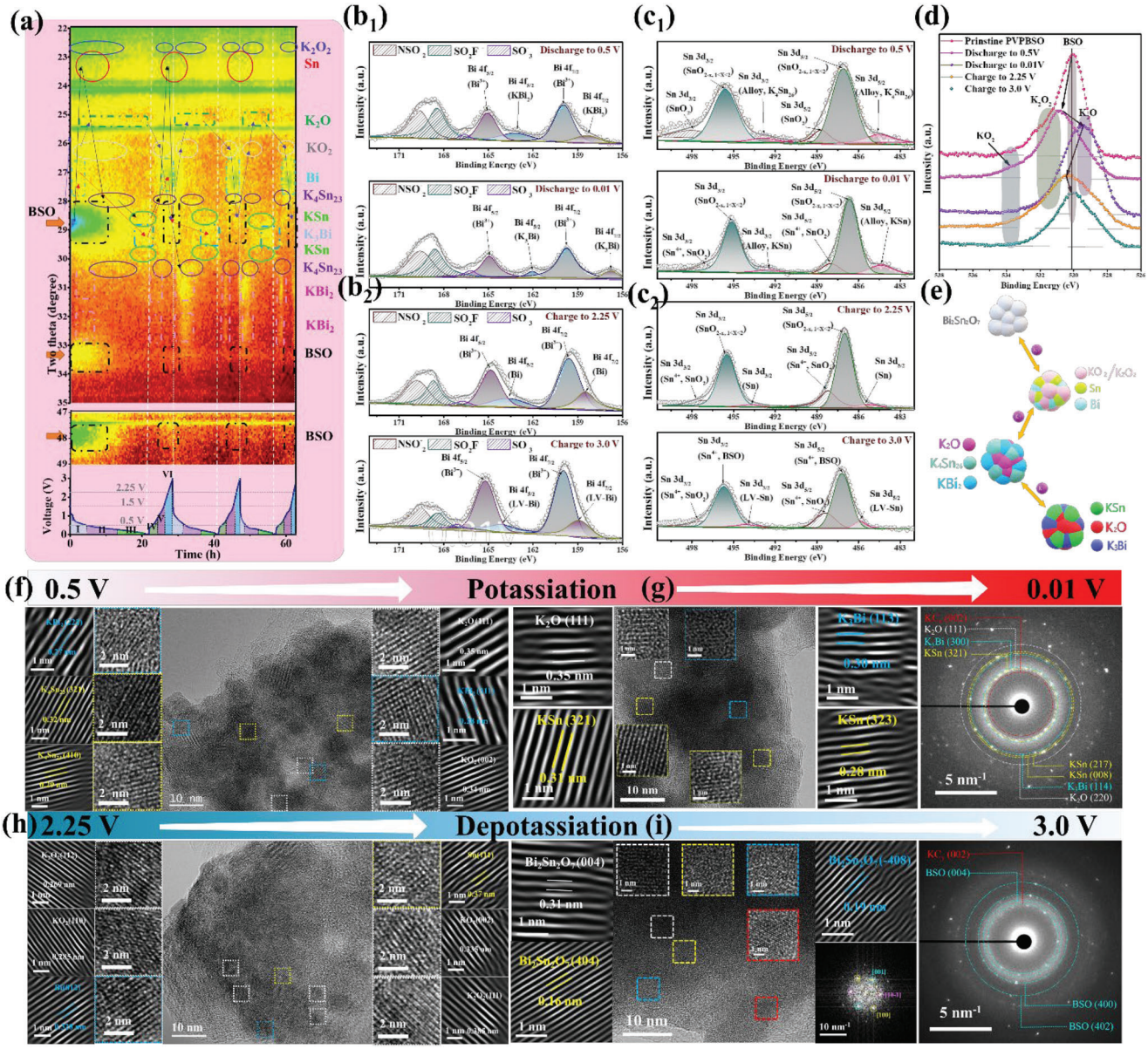

Figure 4. Operando and ex situ analysis of K-ions storage mechanism of PVPBSO/mWFG. a) Contour pattern of the operando XRD ranged from 22° to 49° with corresponding GCD curves for initial three cycles. b,c) Ex situ XPS analysis of Bi 4f and Sn 3d of PVPBSO/mWFG at certain discharge–charge voltages. d) Ex situ XPS spectra of O 1s of PVPBSO. e) Schematic illustration of the K^+ storage mechanism of conversion-alloying reactions. f–i) Post-mortem HRTEM analysis of PVPBSO/mWFG at potassiation state of 0.5 and 0.01 V as well as depotassiation state of 2.25 and 3.0 V, respectively.

of SnO_{2-x} would shift with that of Sn0 on the condition of a fixed position of SnO_4 originating from the air-oxidized surface, similar to the fixed signal of the electrolyte in the Bi 4f spectrum. The binding energies of Sn metal (493.6/485 eV) and Sn (494.2/485.9 eV) of PVPBSO lattice at 2.25 and 3.0 V, respectively, demonstrate the reversible BSO crystal structure. While charging to 2.25 V, the reverse conversion reaction has been conducted and formed the K_2O_2 and KO_2 from K_2O phase shown in Figure 4d. At initial discharge voltage of 0.5 V and charge voltage of 2.25 V, the O 1s spectrum exhibits the broad peaks consisted of KO_2 (≈534.0 eV), K_2O_2 (531–532 eV), and K_2O (529.0–530.0).[50,51] The sharper XPS peak centered at ≈529 eV when discharged to 0.01 V confirms the existence of K_2O. Meanwhile, the XPS peak shifts back to a binding energy of ≈530 eV upon charging to 3.0 V, indicating the presence of the BSO phase. By combining operando XRD with ex situ XPS analysis, the electrochemical evolution scheme is illustrated in Figure 4e. The phase evaluation of PVPBSO and post-mortem morphologies at specific voltages are displayed in Figure 4f–i. The yellow, blue, and white dashed frames designate Sn-, Bi-, and O-based intermediates, respectively. Products of conversion and alloying reactions at each stage can be distinguished through ex situ TEM images and corresponding SAED patterns, in accordance with operando XRD and ex situ XPS. As discharged to the cut-off voltage of 0.01 V, the

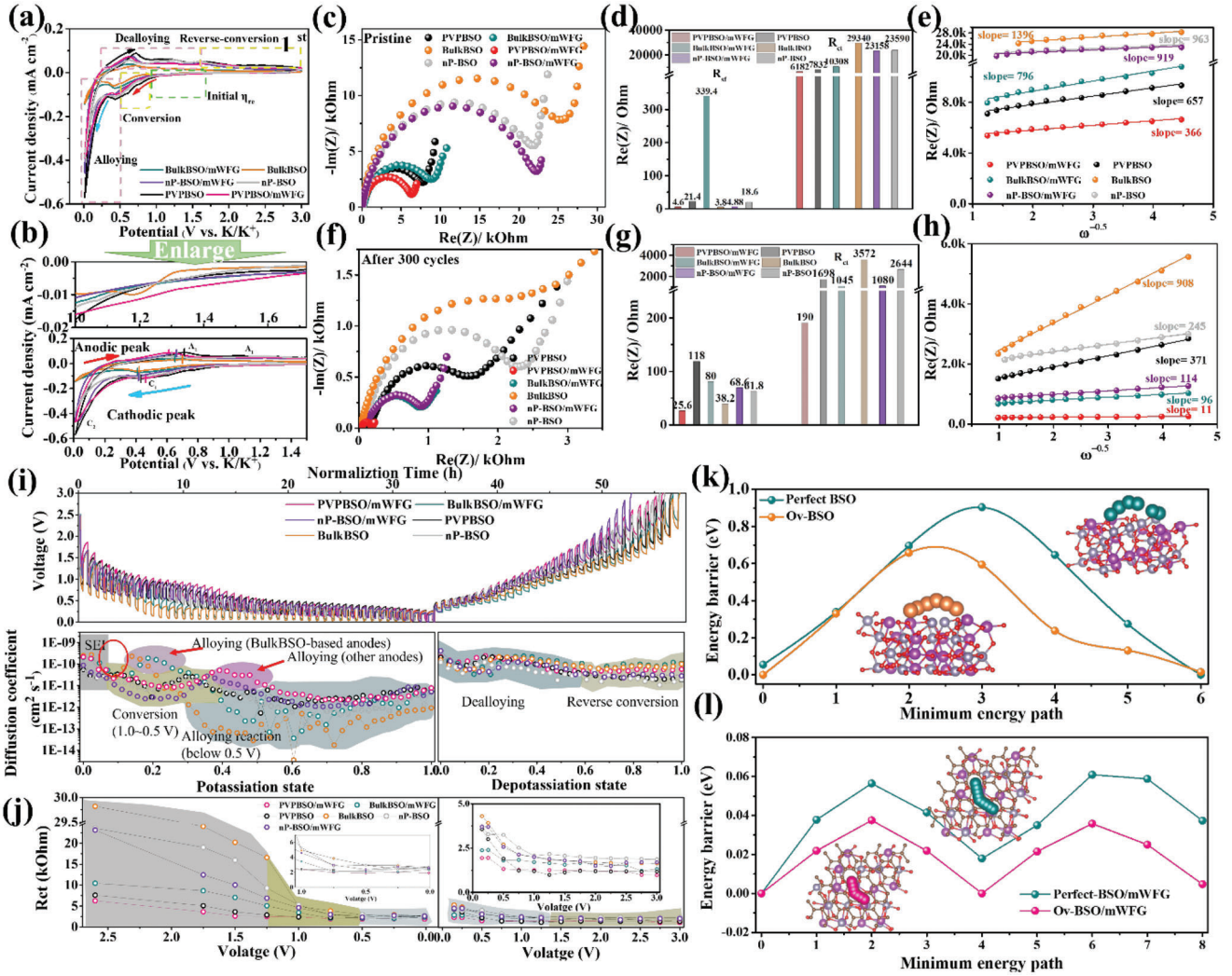

Figure 5. Electrochemical kinetic behaviors and simulations of PVPBSO/mWFG. a) Cyclic voltametric curves of host materials and others in this work at scan rate of 0.1 mV s^{-1} for initial cycling. b) Enlarged CV curves of (a). c,f) Nyquist plots, d,g) fitted R_{sf} and R_{ct}, and e,h) linear diagram for Warburg factor before and after cycling process. g) GITT measurement with 15 min current pulse of 50 mA g^{-1} followed by relaxation time of 30 mins and i) calculated diffusion coefficients of each current pulse. j) In-situ EIS and calculated R_{ct} values at 50 mA g^{-1}. NEB simulation of diffusion energy barriers of k) Perfect-BSO and Ov-BSO, as well as l) Perfect-BSO/mWFG and Ov-BSO/mWFG.

d-spacings of K_3Bi (113), KSn (321)/(323), and K_2O (111) are 0.3, 0.31, 0.28, and 0.35 nm (Figure 4g and Figure S26, Supporting Information), respectively. The SAED pattern further presents K_2O, K_3Bi, and KSn at a discharging voltage of 0.01 V with corresponding lattice planes of (220), (114), and (217)/(008) existing in a large two-theta region, which cannot be well-detected by XRD. At the reverse conversion stage (2.25 V) in Figure 4h and Figure S27 (Supporting Information), lattice planes of related conversion products can be found in the HRTEM image with mask-modified inverse-FFT patterns. Significantly, the 2D lattice of PVPBSO is shown in the red dashed frame and corresponding FFT pattern when charged to 3.0 V (Figure 4i and Figure S28, Supporting Information), proving the existence of a reversible crystal structure of PVPBSO/mWFG. The main lattice fringes of (004), (404), and (−408) of PVPBSO appeared independently with one-dimensional lattice, while the ring pattern presents three lattice planes related to PVPBSO. This continuously enhances the Schottky heterojunction with maintained deficient architecture during sequential cycling tests. The post-mortem images of PVPBSO/mWFG show the well-maintained heterostructure without any cracks or phase separation, confirming the reversibility of PVPBSO crystals and Schottky heterostructure. In addition to the reversibility of PVPBSO/mWFG, the ex situ MS plot of PVPBSO/WFG after 500 cycles proves the sustainability of Schottky junction with the existence of n-type property The reversibility of PVPBSO/mWFG and sustainability of heterojunction effect are complemented, as the PVPBSO materials maintain their semiconducting property after charging to 3.0 V. Despite PVPBSO undergoing a transformation after discharging to 0.01 V, the structural and compositional reversibility of PVPBSO/mWFG, when charged to 3.0 V, continues to uphold the n-type Schottky characteristics in subsequent cycles. The persistent junction effect thereby continually improves and maintains the electrochemical kinetics and

performance of PVPBSO/mWFG, even after extended cycling processes.

The diffraction peak of mWFG, which is different from the reaction of traditional graphite, is located at ≈24° overlapped with stainless-steel device. With the assumption of completed reaction, the corresponding mechanism of each stage is integrated below

Discharge state

$$\text{Stage I: } Bi_2Sn_2O_7 + K^+ + e^- \rightarrow K_2O_2{+}KO_2{+}3K_2O + 2Bi + 2Sn \rightarrow K_2O + 2Bi + 2Sn \ (1^{st}\ \text{discharge, 0.6 V}) \quad (2)$$

$$\text{Stage II: } 2Bi + 23Sn{+}K^+ + e^- \rightarrow KBi_2 + K_4Sn_{23} \ (1^{st}\ \text{discharge, 0.6} - \text{0.25 V}) \quad (3)$$

$$\text{Stage III: } KBi_2 + K_4Sn_{23} + K^+ + e^- \rightarrow 2K_3Bi + KSn \ (1^{st}\ \text{discharge, 0.01 V}) \quad (4)$$

Charge state

$$\text{Stage IV: } K_3Bi + KSn{-}K^+ - e^- \rightarrow KBi_2 + K_4Sn_{23} \ (1^{st}\ \text{charge, 0.8} - \text{0.9 V}) \quad (5)$$

$$\text{Stage V: } KBi_2 + K_4Sn_{23} - K^+ - e^- \rightarrow Bi + Sn \ (1^{st}\ \text{charge, 1.5 V}) \quad (6)$$

$$\text{Stage VI: } Bi + Sn{+}K_2O{-}K^+ - e^- \rightarrow K_2O_2{+}KO_2 + 2Bi + 2Sn \rightarrow Bi_2Sn_2O_7 (1^{st}\ \text{charge, 3.0 V}) \quad (7)$$

In addition, there is a small variation of mWFG fringes (3.36 Å) in Figure S30 (Supporting Information), exhibiting the increased *d*-spacing up to 3.8 Å and decreased *d*-spacing to 3.6 Å during potassiation and depotassiation, respectively. The EDS mapping patterns of PVPBSO/mWFG at specific potentials confirm the uniform distribution of Bi, Sn, O, and C without structural deviation and component separation from Schottky heterojunction, as given in Figure S31 (Supporting Information). After initially charging to 3.0 V, there is still the present of K-element signal, attributing to the SEI layer and reminding of K ions in KC_x. Due to the uniform existence of K ions slightly stored and adsorbed on the PVPBSO/mWFG, for proving the well-contacted heterostructure without cracking, it could be beneficial to enable the feasibility of fast redox reactions for next cycles. In addition, the functional groups of electrolytes, including NSO^{2-}, SO_2F^-, and SO^{3-}, can be identified at binding energies of 169.7, 168.5, and 166.2 eV, respectively.

Furthermore, the weak signal of Sn-based phase confirms that the Sn in PVPBSO lattice cannot be completely reacted in XRD contour plot, leading to the formation of Sn^{4-2x} state in XPS spectrum, thereby maintaining the partial architectural lattice and benefiting to the reversibility of PVPBSO crystal structure upon charging to 3.0 V.

2.5. Electrochemical Kinetic and Diffusion Analysis of Schottky Heterostructures

To deeply investigate positive effect of heterojunction engineering, CV, EIS, and GITT are instrumental in demonstrating the significance of heterointerface formation and efficient junction effects. As illustrated in Figure 5a, the CV curves of anode materials can be divided into five regions based on operando XRD analysis. Initially, the lowest activation overpotential of PVPBSO/mWFG suggests that it facilitates K-ion transport on the anode surface, making it easier to initiate the potassiation reaction (see the upper inset of Figure 5b). The large reactive area of PVPBSO, without orderly junction-mediated charge transfer, can cause an uneven distribution of carriers around the exposed surface and inner spaces, resulting in a nonuniform thickness of the SEI layer with high electrochemical resistance. In other words, both charge accumulation and a thick SEI layer can lead to poor kinetic reactions and slow diffusion behavior. Consequently, ex situ EIS techniques are employed to analyze the electrochemical impedances of pristine and cycled materials in Figure 4c,f, and Note S14 (Supporting Information). In the high-frequency region of pristine materials (Figure 5d and Figure S32a, Supporting Information), the R_{sf} of BulkBSO/mWFG is larger than that of other anodes. This is because the bulk materials cause disordered structures and aggregation of mWFG during the ball-milling process, resulting in poor conductivity and a nonideal heterointerface with weak Schottky-junction effects.[52] Due to the formation of an insulator layer induced by a poor heterojunction, the mWFG cannot effectively integrate electron transport orientation. Despite the presence of nanoengineering and deficient architecture, the R_{sf} of bare materials is higher than that of heterostructures (PVPBSO/mWFG and nP-BSO/mWFG) due to the absence of junctions. In the medium-frequency region, a well-contacted heterostructure can enhance charge transport from the passivating layer to active materials. The reduced R_{ct} of heterostructures demonstrates that both carriers have been accelerated once the Schottky junction forms. The large transport barrier (>20 000 Ω) and small difference (432 Ω) between nP-BSO and nP-BSO/mWFG indicate that even though the materials have been fabricated using a nanosized synthesis process, it cannot improve charge transfer on the surface of nP-BSO and mWFG. A significant decrease in the R_{ct} of BulkBSO/mWFG implies that nonuniform distribution of mWFG not only raises the R_{sf} but also expands the interspace between BulkBSO and mWFG, subsequently lowering the charge transfer barrier. Thanks to the synergy of Schottky junction and OVs, pristine PVPBSO/mWFG performs the best transfer capability of electrons and K ions with lowest R_{ct}.

The tendency of slopes related to Warburg impedance (σ) is similar to that of R_{ct}, implying that the PVPBSO/mWFG delivers a best diffusion capability with small σ, whereas the BulkBSO shows the highest diffusion resistance ($\sigma_{BulkBSO} = 1396$) (Figure 5e). Most importantly, after 300 cycles chosen from the long-term cycling test (Figure 5f), the surface film resistance (R_{sf}) of each anode increases at the solid–liquid interface due to electrolyte consumption, which is a result of the growth of the SEI layer surrounding the exposed surface area. An appropriate thickness and uniformity of SEI films can prevent continuous electrolyte consumption, facilitate K-ion transport with

decreased charge transfer barrier. The substantial R_{sf} of PVPBSO and nP-BSO indicates a nonideal SEI film, which is due to the extensive exposed reactive surface stemming from the nanoengineering design. In the absence of unintegrated electron transfer, SEI films could not only develop on the mWFG surface but also deposit within the internal mWFG layers, resulting in the formation of dual passivating films. Moreover, the R_{ct} of all materials decreases because the materials become activated during the cycling process. Except for the host heterostructure, the R_{ct} values of other materials exceed 1000 Ω, representing a substantial resistance that results in increased overpotential and polarization. Specifically, both R_{sf} and R_{ct} of PVPBSO/mWFG are much smaller compared to other anodes (Figure 5g and Figure S32b, Supporting Information), benefiting from the OV-amplified Schottky heterojunction coupled with an inversion layer. Therefore, the oriented bipolar carriers transfer to the exterior surface and heterointerface without electron tunneling.[53] Electrons moving from PVPBSO to mWFG are uniformly dispersed along the mWFG's delocalization surface, enhancing the formation of a sturdy SEI film that stabilizes the active surface and lowers the R_{sf}. As carrier inversion takes place in the SCR, the electric hole carriers within the inversion layer aid K-ion diffusion in PVPBSO, resulting in high ionic conductivity and enabling complete conversion-alloying reactions of PVPBSO/mWFG. Consequently, the diffusion impedance of PVPBSO/mWFG is the lowest among the materials shown in Figure 5h.

GITT and in-situ EIS tests further emphasize the necessity of Schottky junction in Figure 4i,j. According to the reaction plateaus of the GITT voltage profile, the gray, yellow, and blue regions represent the solid–liquid reaction, conversion reaction, and alloying reaction, respectively, while the light and dark pink regions indicate the starting points of the alloying reaction for BulkBSO-based and other materials, respectively, due to their different plateau lengths. As redox reactions occur, K ions must insert from the surface to inner active sites, altering the K-ion diffusion barrier with variations in redox plateaus, active material utilization, and extraction of transition-state products. As the SEI film progressively grows on active materials, the diffusion coefficients of all materials slightly decrease due to the Faradaic reaction, while the R_{ct} values decrease with gradually unlocked ionic and electronic channels, including the interface between electrolyte and SEI layer, SEI layer and mWFG, as well as mWFG and metal oxide.[54,55] As conversion reaction begins, diffusivities decrease and then increase after Bi and Sn metal extraction. In addition, due to the low reactivity and utilization of conversion species, the diffusion coefficients of BulkBSO-based materials are only shown in the red circle, leading to the alloying reaction starting sooner than for other anodes, as indicated by the first red arrow. With the continuous insertion of K ions, diffusivities decline through two alloying stages. In the depotassiation process, the trends of diffusion coefficients and plateau variation are similar to those in the potassiation state. Remarkably, PVPBSO/mWFG maintains stable and fast K-ion transport ability with higher diffusivity ranging from 10^{-9} to 10^{-11} cm^2 s^{-1}, emphasizing the positive effect of the optimized Schottky heterojunction with carrier inversion around the SCR. Furthermore, the R_{ct} of PVPBSO/mWFG remains consistently lower than that of other materials throughout the initial discharge and charge processes, indicating that low electron/ion transfer resistance enables efficient reactions within PVPBSO/mWFG (enlarged Figure 5j). In agreement with ex situ EIS, the host material exhibits the expected kinetic/diffusion behaviors and wide-and-high plateaus, achieving high K-ion diffusivity regardless of solid–liquid interface, conversion, and alloying reactions. Although nanosized and heterostructure designs improve electrochemical performance compared to bulk and bare materials, an inevitable charge transfer barrier and sluggish diffusion behavior still result in poor rate capability and a short lifespan.

To support the proof-of-concept experiment, nudged elastic band (NEB) simulations are employed to calculate the minimum energy paths and demonstrate the diffusion ability of K ions across defect and perfect regions. As shown in Figure 5k, the absence of high-EN oxygen atoms reduces the K-ion adsorption energy of BSO surface, lowering the surface energy barrier and enhancing K-ion diffusivity across the deficient site. The overall energy barriers of Ov-BSO are lower than those of Perfect-BSO, implying that the higher the vacancy concentration in BSO, the better the K-ion diffusion capability. Consequently, PVPBSO has lower R_{ct} and Z_w at OCP and initial discharge states compared to other materials, except for PVPBSO/mWFG. Stacking a single-layered mWFG on the BSO surface simulates the metal–semiconductor junction effect, as shown in Figure 5l. With the removal of an oxygen atom, unpaired electrons form and transfer from the deficient region to mWFG, enhancing electric/ionic mobility and conductivity, thereby facilitating the driving force of K-ion transport and reducing diffusion barriers. The diffusion barriers of Ov-BSO/mWFG are much smaller than those of Perfect-BSO, confirming the reliable synergy of interfacial chemistry and defect engineering.

2.6. Discussion and K-Ion Full-Cell Demonstration

The main features of PVPBSO/mWFG are Schottky heterojunctions with acquired bipolar-junction-enhanced carrier transport, indicated through the following aspects: i) Low oxidation state of Sn and Bi mediated by Interface chemistry decrease the WF and EA of n-type BSO, thereby enhancing the electron donor ability to high-work-function mWFG. The increased interface dipole between metal and semiconductor, induced by abundant OVs, intensifies the driving force of carrier transfer. The EPR spectra, HAADF-STEM image, and Raman spectrum, as well as Bader analysis confirmed the existence of OVs and bond-disconnected position. ii) The sufficient built-in voltage and band-bending phenomena result in majority carrier inversion of BSO near the SCR of heterointerface. Electrons act as the major carrier in n-type semiconductors, while the electric holes are the charge carrier in p-type semiconductors. Combined with the UPS, UV–vis, and MS plot with DFT simulation, the band diagrams are constructed consist of WF, EA, VBM, CBM, bandgap, built-in voltage, and interface dipole. iii) Electron tunneling can be prevented through an adequate and suitable width and height of Schottky barrier. Efficiently controlling the charge-migrated direction can facilitate an effective conversion-alloying reaction without blocking K ions transfer and diffusion, thereby forming a strong Schottky junction. The width and height of Schottky barrier as well as the direction of charge transport are crossly verified through

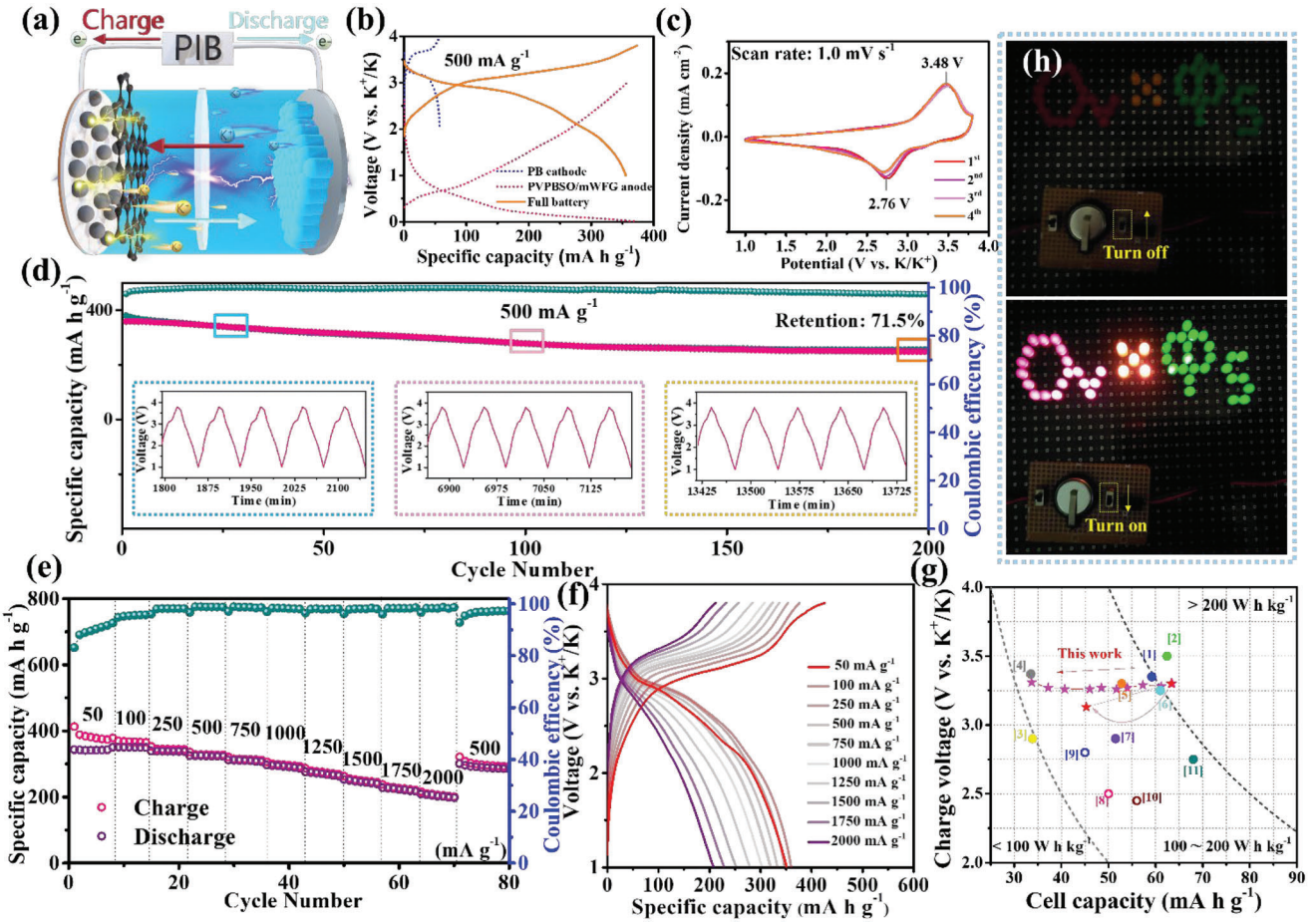

Figure 6. Electrochemical performances and practical application of PVPBSO/mWFG//PB. a) Scheme of PIB full battery. b) GCD curves of cathode, anode, and a full battery. c) CV curves of full battery at scan rate of 1.0 mV s^{-1}. d) Long-term cycling performance based on active material of anode at 500 mA g^{-1}. The inset shows the voltage profiles at specific cycles. e) Rate performance at various current densities of 50–2000 mA g^{-1} and f) corresponding GCD curves. g) Full-cell comparison with other literatures. h) Digital images of lighting test with three types of LED bulbs.

photoemission spectrums in tandem with ESP and CDD simulation. Due to the sufficient Schottky barrier and interface polarization resulted from OVs on PVPBSO exposed surface, the acquired p-type semiconducting property of PVPBSO/mWFG can effectively enhance the diffusivity of K ions through the heterointerface of PVPBSO side. iv) Structural and component reversibility consistently support the existence of junction effect during cycling process, therefore, the overpotentials and polarization of each potassiation state have been reduced and maintained even after 500 cycles. Thanks to above-mentioned merits, the Schottky heterostructure have been reinforced with a suitable growth of SEI film, decreasing the electrochemical impedances (i.e., R_{sf} and R_{ct}) and expediting the adsorption and diffusion of K ions inside the PVPBSO/mWFG. Consistent with NEB calculation of K ions diffusion path, the in-situ kinetic measurements (i.e., GITT and EIS) demonstrate the excellent transport ability of K ions through the PVPBSO/mWFG, beneficial from the orderly Schottky-controlled electron transfer. Due to the comprehensive analysis and evidence, the PVPBSO/mWFG could be significantly proved for owning an outstanding cyclability and rate performances, accompanied by highly reactive architecture and reversible retention.

We demonstrate the assembly of PIB full cells PVPBSO/mWFG anode with PB cathode (**Figure 6**a). The PB contributes a reversible capacity of 60 mA h g^{-1} with great overlapped voltage curves (Figure S33, Supporting Information). The reason for consideration of using PB-based material is attached in Note S15 (Supporting Information). Typical GDC profiles of the PVPBSO/mWFG//PB full cell in Figure 6b at a current density of 500 mA g^{-1}, based on the mass loading of active materials of the anode, demonstrate a capacity similar to PVPBSO/mWFG half cells. Notably, multiple redox reactions in PVPBSO/mWFG perform a considerable capacity (pink line), while the PB cathode provides a paired redox plateau at voltages of 3.66 and 3.20 V. Due to the comparable areal capacity of negative and positive electrodes, the capacity contributions of the full battery show a mixture of anodic and cathodic reactions of both electrodes. To distinguish the charge and discharge plateaus of the full cell, the CV analysis clearly displays the highest charge and lowest discharge plateaus, as shown in Figure 6c, in good agreement with the GDC curve of the full cell. This demonstrates the potential of PVPBSO/mWFG for use in full PIBs, improving safety and performance for commercial applications. The long-term cycling performance of the PVPBSO/mWFG//PB full cell demonstrates

a stable retention of 71.5% after 200 cycles at a current density of 500 mA g^{-1} based on the active materials of the anode, with an initial capacity of around 380 mA h g^{-1} (Figure 6d). The corresponding voltage profiles (insets of Figure 6d) indicate excellent reversibility of the full cell at the 25th, 100th, and 200th cycles. The PVPBSO/mWFG//PB full cell delivers reversible capacities at various current densities (Figure 6e,f), achieving a high energy density of 209.6 Wh kg^{-1} and a power density up to 6620 W kg^{-1}, calculated based on the total active materials of both electrodes according to a previous calculation method. Energy densities, cell capacities, and charge voltages are compared with other literature in Figure 6g and Table S3 (Supporting Information).[3,6,56–63] The major oxidation plateaus with a voltage of 3.48 V successfully lights different voltage-supplied and 49 LED bulbs, proving the sufficient energy density and potential output of the PVPBSO/mWFG//PB full cell (Figure 6h and Figure S34, Supporting Information). The excellent performance of the PVPBSO/mWFG//PB full cell is attributed to the reversible conversion-alloying reactions, which are enhanced by optimized heterointerface synergy. This cell outperforms organic and layered oxide-based full batteries in terms of oxidation plateaus, which can be attributed to the use of PB-based cathodes.

3. Conclusions

In summary, PVPBSO with abundant OVs was constructed with mWFG through amplifying Schottky effect, greatly enhancing the built-in voltage and charge transfer. The electrochemical kinetics and reversibility of the conversion reaction are significantly enhanced by the sufficient network contacting the heterogeneous interface, as verified by both experiments and simulations. Due to abundant Ov sites, the PVPBSO establishes a large difference of interface dipole related to mWFG, significantly producing a strong driving force of electron transfer. Therefore, a favorable inversion of majority carriers in SCR is inspired, decreasing the charge transfer impendence and diffusion barrier, thereby relieving the redox overpotential and polarization. The construction of the Schottky heterojunction and acquired p-type semiconducting property form the built-in electric field between PVPBSO and mWFG, providing an efficient shortcut for lateral K ions transport and vertical electron transfer. The systematic movement of bipolar carriers enhances the passage of electrons and potassium ions through the heterostructure's interior and exterior surfaces. This is accompanied by reversible redox reactions, as confirmed by both operando and ex situ analyses. Even after long-term cycling process, the kinetic barriers of PVPBSO/mWFG are the smallest compared to those of other anodes without strong Schottky junction. Notably, the PIB full cell of PVPBSO/mWFG//PB contributed a sufficient energy density with great cyclability and rate capability due to the high oxidation plateau and cell capacity. This work provided not only a strategy for constructing high-performance Schottky heterostructure with effective carrier transfer, but also new avenues toward achieving thorough analysis of heterojunction through proof-of-concept experiments.

4. Experimental Section

Fabrication of PVPBSO: In a typical synthesis, first, 2 mmol (0.970 g) $Bi(NO_3)_3$ (Sigma-Aldrich, >98%) and 2 mmol (0.598 g) K_2SnO_3 (Alfa Aesar, 99.4%) were uniformly dispersed in 50 mL deionized water stirred with 500 rpm and sequentially ultrasonic treatments at room temperature. Second, 2 g PVP stabilizer (Sigma-Aldrich, MW = 55 000) was added into the solution contained Bi and Sn precursors and stirred for 30 min. After completely forming a homogeneous solution, the pH of the solution was adjusted to 12 by 1.5 mL 2 M NaOH. After stirred for 20 min, the mixed solution was transferred into 100 mL Teflon autoclave at 200 °C for 20 h. The gray PVPBSO was collected by centrifugation with 30 ml DI water for several times and 30 ml ethanol for the last times.

Fabrication of BSO: 2 mmol (0.970 g) $Bi(NO_3)_3$ and 2 mmol (0.598 g) K_2SnO_3 were uniformly dispersed in 50 mL deionized water stirred with 500 rpm and sequentially ultrasonic treatments at room temperature. After forming a homogeneous solution, the pH of the solution was adjusted to 12 by 1.5 mL 2 M NaOH. After stirred for 20 min, the mixed solution was transferred into 100 mL Teflon autoclave at 200 °C for 20 h. The yellow BSO was collected by centrifugation with 30 mL deionized water for several times and 30 mL ethanol for the last times.

Fabrication of BulkBSO: 1 mmol (0.466 g) Bi_2O_3 with 2 mmol (0.301 g) SnO_2 were uniformly dispersed in 10 mL EtOH solution under ultrasonic treatments. After evaporation, the powder was transferred to porcelain crucible and calcined in a muffle furnace at 750 °C for 24 h at a heating rate of 3 °C min^{-1}.

Fabrication of mWFG: 100 mg traditional graphite was placed in a stainless-steel ball-milling jar, and the mixture was milled at 200 rpm for 15 h under argon protection using a high-energy grinding mill (RETSCH PM100).

Fabrication of Schottky Heterostructures: 75 mg of BSO powder and 25 mg of mWFG were placed in a stainless-steel ball-milling jar, and the mixture was milled at 200 rpm for 15 h under argon protection using a high-energy grinding mill. The weight ratio of grinding balls/mixture powder was 20:1.

Fabrication of PB Cathode: A modified coprecipitation method was adopted to synthesize the cathode materials. Solution A was prepared as follows: 3 mmol (0.596 g) of $FeCl_2{\cdot}4H_2O$ (Sigma-Aldrich, 98%) was dissolved in 50 mL of deionized water. Solution B was prepared as follows: 5 mmol (2.1 g) of $K_4Fe(CN)_6{\cdot}3H_2O$ (Sigma-Aldrich, 99.5%), 10 mmol of potassium citrate, and 12 g of KCl (PubChem, 99%) were dissolved in 100 mL of deionized water. Solution A was slowly added into solution B and maintained at RT for 4 h. The blue powder was centrifugalized and washed several times with deionized water and EtOH, and finally dried at 80 °C in a vacuum furnace for 2 h.

Electrochemical Measurements—Preparation of Anodes and Cathodes: These electrodes were prepared by mixing the anode materials (70%), super-P (20%), and NaCMC (10%) in deionized water to form a uniform slurry. The homogeneous slurry was coated onto the copper foil and dried in a furnace at 80 °C under argon flow to remove the residual solvent. The mass loading of active material is 0.8–1.0 mg cm^{-2} for half cells using a microbalance with 0.1 µg resolution (Sartorius SE2). These electrodes were prepared by mixing the PB (70%), super-P conductive agent (20%), and PVDF (10%) in NMP solvent, which was added into a plastic jar and put into ball mill machine rotated at 350 rpm for 15 min. The homogeneous slurry was coated on to the aluminum foil and dried inside a furnace at 80 °C under argon flow to remove the residual solvent.

Electrochemical Measurements—Potassium-Ion Half Cells Assembly of Anode and Cathode Materials: The electrochemical performance of the electrodes was tested in the CR2032 coin-type half cells with the handmade potassium metal foil as the counter electrode. The electrolyte used in the cells was 1 M KFSI in DMC. The cells were assembled in an argon-filled glove box with both the moisture and the oxygen content bellow 1 ppm (M. Braun UNILAB). The CV and EIS curves were obtained on Bio-Logic-Science Instruments, VMP3 workstation. Galvanostatic discharge–charge tests were evaluated by NEWARE CT-4000 battery measurement system from 0.01–3.0 V (anode) and 2.0–4.0 V (cathode) versus K/K^+.

Electrochemical Measurements—Potassium-Ion Full Cells of PVPBSO/mWFG//PB: The CR2032 coin-type full cell for battery was assembled by using PVPBSO/mWFG//PB as anode and PB as cathode with anode/cathode ratio of 1:5 (wt%) under argon environment. Both electrodes were pre-potassiated for 25 cycles before the full cell assembly, and 1 M

KFSI in DMC was used as electrolyte. Galvanostatic discharge–charge tests were evaluated by NEWARE CT-4000 battery measurement system from 1.0 to 3.8 V versus K^+/K.

Supporting Information

Supporting Information is available from the Wiley Online Library or from the author.

Acknowledgements

This work was supported by the financial support from the 2030 Cross-Generation Young Scholars Program by National Science and Technology Council, Taiwan (NSTC 112-2628-E-007-010 & NSTC 112-2628-E-007-016). The authors thank the technical support from Ms. Y. M. Chang in Instrumentation Center at National Tsing Hua University.

Conflict of Interest

The authors declare no conflict of interest.

Author Contributions

Y.-Y.H.: conceptualization, methodology, data curation, writing; H.-Y.T.: conceptualization, resources, supervision, writing – review & editing.

Data Availability Statement

The data that support the findings of this study are available from the corresponding author upon reasonable request.

Keywords

heterostructures, oxygen vacancy, potassium-ion batteries, Schottky junction

Received: June 26, 2023
Revised: August 4, 2023
Published online:

[1] R. Rajagopalan, Y. Tang, X. Ji, C. Jia, H. Wang, *Adv. Funct. Mater.* **2020**, *30*, 1909486.
[2] Z. Jian, Z. Xing, C. Bommier, Z. Li, X. Ji, *Adv. Energy Mater.* **2016**, *6*, 1501874.
[3] C.-H. Chang, K.-T. Chen, Y.-Y. Hsieh, C.-B. Chang, H.-Y. Tuan, *ACS Nano* **2022**, *16*, 1486.
[4] S.-B. Huang, Y.-Y. Hsieh, K.-T. Chen, H.-Y. Tuan, *Chem. Eng. J.* **2021**, *416*, 127697.
[5] F.-W. Yuan, H.-J. Yang, H.-Y. Tuan, *J. Mater. Chem.* **2011**, *21*, 13793.
[6] P. Xiong, J. Wu, M. Zhou, Y. Xu, *ACS Nano* **2019**, *14*, 1018.
[7] H.-J. Yang, C.-Y. Chen, F.-W. Yuan, H.-Y. Tuan, *J. Phys. Chem. C* **2013**, *117*, 21955.
[8] N. Kapuria, S. Imtiaz, A. Sankaran, H. Geaney, T. Kennedy, S. Singh, K. M. Ryan, *Nano Lett.* **2022**, *22*, 10120.
[9] H. Wu, S. Lu, S. Xu, J. Zhao, Y. Wang, C. Huang, A. Abdelkader, W. A. Wang, K. Xi, Y. Guo, *ACS Nano* **2021**, *15*, 2506.
[10] C.-Y. Tsai, C.-H. Chang, T.-L. Kao, K.-T. Chen, H.-Y. Tuan, *Chem. Eng. J.* **2021**, *417*, 128552.
[11] W.-C. Lin, Y.-C. Yang, H.-Y. Tuan, *Energy Storage Mater.* **2022**, *51*, 38.
[12] W. C. Lin, Y. C. Yang, H. Y. Tuan, *Small* **2023**, *19*, 2300046.
[13] C.-B. Chang, Y.-R. Lu, H.-Y. Tuan, *Energy Stor. Mater.* **2023**, *59*, 102770.
[14] W.-W. Shen, Y.-Y. Hsieh, H.-Y. Tuan, *J. Colloid Interface Sci.* **2023**, *643*, 626.
[15] W. Feng, H. Wang, Y. Jiang, H. Zhang, W. Luo, W. Chen, C. Shen, C. Wang, J. Wu, L. Mai, *Adv. Energy Mater.* **2022**, *12*, 2103343.
[16] D. Qiu, B. Zhang, T. Zhang, T. Shen, Z. Zhao, Y. Hou, *ACS Nano* **2022**, *16*, 21443.
[17] Y.-Y. Hsieh, K.-T. Chen, H.-Y. Tuan, *Chem. Eng. J.* **2021**, *15*, 130451.
[18] T. Li, Y. Wang, Q. Zhou, L. Yuan, S. Qiao, M. Ma, Z. Liu, S. Chong, *J. Mater. Sci. Technol.* **2023**, *158*, 86.
[19] K.-T. Chen, S. Chong, L. Yuan, Y.-C. Yang, H.-Y. Tuan, *Energy Storage Mater.* **2021**, *39*, 239.
[20] S.-F. Ho, H.-Y. Tuan, *Chem. Eng. J.* **2023**, *452*, 139199.
[21] M. Huang, B. Xi, L. Mi, Z. Zhang, W. Chen, J. Feng, S. Xiong, *Small* **2022**, *18*, 2107819.
[22] Y.-Y. Hsieh, H.-Y. Tuan, *Energy Storage Mater.* **2022**, *51*, 789.
[23] J. Tang, C.-Y. Wang, F. Xiu, A. J. Hong, S. Chen, M. Wang, C. Zeng, H.-J. Yang, H.-Y. Tuan, C.-J. Tsai, *Nanotechnology* **2010**, *21*, 505704.
[24] Y.-Y. Hsieh, H.-Y. Tuan, *Mater. Today Sustainability* **2022**, *18*, 100141.
[25] C. Zhang, H. Li, X. Zeng, S. Xi, R. Wang, L. Zhang, G. Liang, K. Davey, Y. Liu, L. Zhang, *Adv. Energy Mater.* **2022**, *12*, 2202577.
[26] T. Yajima, Y. Hikita, M. Minohara, C. Bell, J. A. Mundy, L. F. Kourkoutis, D. A. Muller, H. Kumigashira, M. Oshima, H. Y. Hwang, *Nat. Commun.* **2015**, *6*, 6759.
[27] T. Miyakawa, T. Harada, S. Ito, A. Tsukazaki, *J. Appl. Phys.* **2020**, *128*, 025302.
[28] R. E. A. Ardhi, G. Liu, J. Park, J. K. Lee, *Energy Storage Mater.* **2023**, *54*, 863.
[29] Y. Liu, X. Zhou, Z. Jia, H. Wu, G. Wu, *Adv. Funct. Mater.* **2022**, *32*, 2204499.
[30] J. Wu, F. Huang, X. Lü, P. Chen, D. Wan, F. Xu, *J. Mater. Chem.* **2011**, *21*, 3872.
[31] R. T. Tung, *Appl. Phys. Rev.* **2014**, *1*, 011304.
[32] A. Vilan, D. Cahen, *Chem. Rev.* **2017**, *117*, 4624.
[33] Y. Lu, M. Chen, T. Huang, Y. Huang, J.-j. Cao, H. Li, W. Ho, S. C. Lee, *Environ. Sci.: Nano* **2021**, *8*, 1927.
[34] Y. Zhang, J. Di, X. Qian, M. Ji, Z. Tian, L. Ye, J. Zhao, S. Yin, H. Li, J. Xia, *Appl. Catal., B* **2021**, *299*, 120680.
[35] S. Gao, R. Wu, M. Sun, M. Guo, D. B. DuBois, S. Chen, H. Ji, C. Wang, Q. Wang, *Appl. Catal., B* **2023**, *324*, 122260.
[36] R. Silva, C. Paschoal, R. Almeida, M. C. Castro, Jr., A. Ayala, J. T. Auletta, M. W. Lufaso, *Vib. Spectrosc.* **2013**, *64*, 172.
[37] W. Gao, Z. Li, Q. Han, Y. Shen, C. Jiang, Y. Zhang, Y. Xiong, J. Ye, Z. Zou, Y. Zhou, *Chem. Commun.* **2022**, *58*, 9594.
[38] R. Garg, N. K. Dutta, N. R. Choudhury, *Nanomaterials* **2014**, *4*, 267.
[39] E. Rut'kov, E. Afanas' eva, N. Gall, *Diamond Relat. Mater.* **2020**, *101*, 107576.
[40] Q. Peng, C. Si, J. Zhou, Z. Sun, *Appl. Surf. Sci.* **2019**, *480*, 199.
[41] L. Chen, H. Li, H. Li, H. Li, W. Qi, Q. Zhang, J. Zhu, P. Zhao, S. Yang, *Appl. Catal., B* **2022**, *318*, 121863.
[42] Z. Zhou, X. Niu, Y. Zhang, J. Wang, *J. Mater. Chem. A* **2019**, *7*, 21835.
[43] C. Si, Z. Lin, J. Zhou, Z. Sun, *2D Mater.* **2016**, *4*, 015027.
[44] J. Wang, X. Zhou, M. Yang, D. Cao, X. Chen, H. Shu, *J. Mater. Chem. C* **2020**, *8*, 7350.
[45] M. T. Greiner, L. Chai, M. G. Helander, W. M. Tang, Z. H. Lu, *Adv. Funct. Mater.* **2012**, *22*, 4557.
[46] R. Har-Lavan, D. Cahen, *IEEE J. Photovoltaics* **2013**, *3*, 1443.

[47] N. Sai, R. Gearba, A. Dolocan, J. R. Tritsch, W.-L. Chan, J. R. Chelikowsky, K. Leung, X. Zhu, *J. Phys. Chem. Lett.* **2012**, *3*, 2173.
[48] U. S. Meda, L. Lal, M. Sushantha, P. Garg, *J. Energy Storage* **2022**, *47*, 103564.
[49] M. Gu, A. M. Rao, J. Zhou, B. Lu, *Energy Environ. Sci.* **2023**, *16*, 1166.
[50] R. Shi, W. Liao, P. J. Ramírez, I. Orozco, M. Mahapatra, J. Kang, A. Hunt, I. Waluyo, S. D. Senanayake, P. Liu, *Angew. Chem.* **2022**, *134*, e202208666.
[51] B. Lamontagne, F. Semond, D. Roy, *J. Electron. Spectrosc. Relat. Phenom.* **1995**, *73*, 81.
[52] C. Ding, L. Huang, J. Lan, Y. Yu, W. H. Zhong, X. Yang, *Small* **2020**, *16*, 1906883.
[53] S. M. Sze, Y. Li, K. K. Ng, *Physics of Semiconductor Devices*, Wiley, New York **2021**.
[54] X.-B. Cheng, C. Yan, X.-Q. Zhang, H. Liu, Q. Zhang, *ACS Energy Lett.* **2018**, *3*, 1564.
[55] X. Y. Yue, Y. X. Yao, J. Zhang, S. Y. Yang, Z. Li, C. Yan, Q. Zhang, *Adv. Mater.* **2022**, *34*, 2110337.
[56] Y. Xu, C. Zhang, M. Zhou, Q. Fu, C. Zhao, M. Wu, Y. Lei, *Nat. Commun.* **2018**, *9*, 1720.
[57] S. Chong, L. Sun, C. Shu, S. Guo, Y. Liu, W. A. Wang, H. K. Liu, *Nano Energy* **2019**, *63*, 103868.
[58] X. Xiang, D. Liu, X. Zhu, K. Fang, K. Zhou, H. Tang, Z. Xie, J. Li, H. Zheng, D. Qu, *Appl. Surf. Sci.* **2020**, *514*, 145947.
[59] J. Liao, Q. Hu, Y. Yu, H. Wang, Z. Tang, Z. Wen, C. Chen, *J. Mater. Chem. A* **2017**, *5*, 19017.
[60] B.-C. Chen, X. Lu, H.-Y. Zhong, P.-W. Huang, Y.-N. Wu, S.-Y. Xu, K.-Z. Du, X.-H. Wu, *J. Mater. Chem. A* **2022**, *10*, 25671.
[61] K.-T. Chen, H.-Y. Tuan, *ACS Nano* **2020**, *14*, 11648.
[62] Z. Tong, R. Yang, S. Wu, D. Shen, T. Jiao, K. Zhang, W. Zhang, C.-S. Lee, *J. Mater. Chem. A* **2019**, *7*, 19581.
[63] Z. Tong, R. Yang, S. Wu, D. Shen, T. Jiao, K. Zhang, W. Zhang, C. S. Lee, *Small* **2019**, *15*, 1901272.